Biophysical *Journal*
Article

Biophysical Society

Selective Interaction of Colistin with Lipid Model Membranes

Fernando G. Dupuy,[1,2] Isabella Pagano,[1] Kathryn Andenoro,[1] Maria F. Peralta,[1,3] Yasmene Elhady,[1] Frank Heinrich,[1,4] and Stephanie Tristram-Nagle[1,*]

[1]Biological Physics Group, Physics Department, Carnegie Mellon University, Pittsburgh, Pennsylvania; [2]Instituto Superior de Investigaciones Biológicas (INSIBIO) CONICET-UNT and Instituto de Química Biológica "Dr Bernabé Bloj", Facultad de Bioquímica, Química y Farmacia, UNT, San Miguel de Tucumán, Argentina; [3]Instituto de Investigación Médica M y M Ferreyra, CONICET-National University of Córdoba, Córdoba, Argentina; and [4]National Institute of Standards and Technology Center for Neutron Research, Gaithersburg, Maryland

ABSTRACT Although colistin's clinical use is limited due to its nephrotoxicity, colistin is considered to be an antibiotic of last resort because it is used to treat patients infected with multidrug-resistant bacteria. In an effort to provide molecular details about colistin's ability to kill Gram-negative (G(−)) but not Gram-positive (G(+)) bacteria, we investigated the biophysics of the interaction between colistin and lipid mixtures mimicking the cytoplasmic membrane of G(+), G(−) bacteria as well as eukaryotic cells. Two different models of the G(−) outer membrane (OM) were assayed: lipid A with two deoxy-manno-octulosonyl sugar residues, and *Escherichia coli* lipopolysaccharide mixed with dilaurylphosphatidylglycerol. We used circular dichroism and x-ray diffuse scattering at low and wide angle in stacked multilayered samples, and neutron reflectivity of single, tethered bilayers mixed with colistin. We found no differences in secondary structure when colistin was bound to G(−) versus G(+) membrane mimics, ruling out a protein conformational change as the cause of this difference. However, bending modulus K_C perturbation was quite irregular for the G(−) inner membrane, where colistin produced a softening of the membranes at an intermediate lipid/peptide molar ratio but stiffening at lower and higher peptide concentrations, whereas in G(+) and eukaryotic mimics there was only a slight softening. Acyl chain order in G(−) was perturbed similarly to K_C. In G(+), there was only a slight softening and disordering effect, whereas in OM mimics, there was a slight stiffening and ordering of both membranes with increasing colistin. X-ray and neutron reflectivity structural results reveal colistin partitions deepest to reach the hydrocarbon interior in G(−) membranes, but remains in the headgroup region in G(+), OM, and eukaryotic mimics. It is possible that domain formation is responsible for the erratic response of G(−) inner membranes to colistin and for its deeper penetration, which could increase membrane permeability.

INTRODUCTION

Colistin (i.e., polymyxin E) was first isolated by Koyama et al. (1) from the broth of *Bacillus polymyxa* in 1949; it is a linear trilipopeptide linked to a cyclic heptapeptide that is produced by nonribosomal peptide synthetase systems in Gram-positive (G(+)) bacteria (2). The fatty acid tail can consist of seven, eight, or nine carbons (3). It has a narrow antibacterial spectrum, mainly against Gram-negative bacteria (G(−)) (4,5), but not G(+) bacteria. Clinical use of colistin decreased in the 1970s due to nephrotoxicity and neurotoxicity after intravenous administration. However, the world is now facing a growing threat from bacteria that are resistant to all available antibiotics (6,7), and colistin has reemerged as an antibiotic of last resort (3), and is in use to treat cystic fibrosis patients. The incidence of resistance to colistin is relatively low (8), but resistance in Gram-negative pathogens can emerge both in vitro (9,10) and clinically (11–14).

Colistin interacts with high affinity with the lipopolysaccharide (LPS) of the outer membrane (OM) of G(−) bacteria (15), which docks the positively charged (+5 e) antibiotic to the cell surface. A critical interaction of colistin with the lipid A component of LPS is suggested by the charge screening mechanism of bacterial resistance whereby negative phosphate charges are neutralized by the addition of aminoarabinose and ethanolamine residues (16). However, membrane blebbing (17) and electrochemical transmembrane potential dissipation in cells treated with colistin have also been reported in previous works (18), which suggests that inner membrane (IM) permeabilization leads to bacterial cell death. What is the mechanism of colistin's rapid, concentration-dependent bacterial killing with negligible postantibiotic effects (10)? Hancock and co-workers (19–23) have proposed a general model for several antimicrobial peptides called the

Submitted August 31, 2017, and accepted for publication December 21, 2017.

*Correspondence: stn@cmu.edu

Editor: Georg Pabst.

https://doi.org/10.1016/j.bpj.2017.12.027

"self-promoted uptake" model, where colistin's aggregation promotes its own uptake across the OM, and subsequent pore formation of the IM. An alternative proposed mechanism is the vesicle-vesicle contact pathway (24,25) where a colistin dimer can mediate the contacts between periplasmic leaflets of inner and outer membranes (24). A third possible mechanism is a generalized mechanism for bactericidal agents, in which an oxidative burst produces a reactive hydroxyl radical (•OH) that can induce rapid cell death (26).

This work aims to delineate the role of lipids in the interactions between colistin and bacterial lipid membrane mimics in an effort to understand the molecular details of colistin's bactericidal mechanism. It is of interest to determine if there are structural or elastic properties that differ between G(+) and G(−) lipid membrane mimics that could be responsible for colistin's preferential killing of G(−) bacteria. As a first approach, we studied the secondary structure of the peptide by means of circular dichroism in the absence and presence of lipid membranes mimicking the outer leaflet (OM) and IM of G(−), cytoplasmic membrane of G(+) bacteria, and eukaryotic cells. With the same membrane mimics, by means of x-ray diffuse scattering we measured both structure (membrane thickness, area/lipid, and peptide position) and the elastic parameter bending modulus (K_C), which yields information about membrane softening. In addition, an order parameter that indicates lipid acyl chain ordering is obtained (S_{xray}). Finally, the third biophysical method, neutron scattering, was used for confirming colistin's location in the membrane mimics. Because our experimental x-ray system is symmetric, we cannot probe the vesicle-vesicle contact model, and we are also not studying oxidized lipids, so we cannot comment on these other two models for bactericidal killing.

MATERIALS AND METHODS

Reagents

The synthetic lyophilized lipids 1-palmitoyl-2-oleoyl-*sn*-glycero-3-phosphoethanolamine (POPE), 1-palmitoyl-2-oleoyl-*sn*-glycero-3-phospho-(1′rac-glycerol) sodium salt (POPG), 1′, 3′-bis[1,2-dioleoyl-*sn*-glycero-3-phospho]-*sn*-glycerol sodium salt (TOCL, i.e., cardiolipin), 1-palmitoyl-2-oleoyl-*sn*-glycero-3-phosphocholine (POPC), 1,2-dioleoyl-3-trimeathylammonium-propane chloride salt (DOTAP), di[3-deoxy-D-manno-octulosonyl]-lipid A ammonium salt (KDO2), and 1,2-dioleoyl-*sn*-glycero-3-[phospho-*rac*-(3-lysyl(1-glycerol))] (chloride salt) (Lysyl PG) were purchased from Avanti Polar Lipids (Alabaster, AL) and used as received. Cholesterol was from Nu-Chek-Prep (Waterville, MN). HPLC grade organic solvents, LPS from *Escherichia coli* 0111:B4, and colistin sulfate salt were purchased from Sigma-Aldrich (St. Louis, MO) and used as received.

Sample preparation

Membrane mimics were prepared by first dissolving lyophilized lipids in chloroform/methanol (8:2, v/v), or LPS in chloroform/methanol/H_2O (2:1:1, v/v/v). Lipid stock solutions were mixed to create lipid mixtures in molar ratios mimicking bacterial membranes: G(−) IM, POPE/POPG/TOCL (7:2:1, molar ratio); G(+) membrane, POPG/DOTAP/POPE/TOCL (6:1.5:1.5:1); and eukaryotic membrane, POPC/POPE/cholesterol (5:1:1.8). For the outer membrane of G(−) bacteria, two different mimics were used: lipid A with two deoxy-manno-octulosonyl sugar residues of the inner core (KDO2), and a mixture of LPS/DLPG (1:3). Stock solutions of colistin (MW = 1400) were prepared in Milli-Q water (Millipore, Billerica, MA).

Multilamellar stacked samples for x-ray scattering were prepared by mixing 4 mg of the different lipid mixtures plus colistin into a glass test tube in various mole ratios from 750:1 to 50:1, lipid/peptide. Solvents were removed by evaporation under vacuum and samples were redissolved in appropriate HPLC-grade solvents for spreading: G(−), G(+), chloroform/trifluoroethanol (TFE) 7:3 (v/v); eukaryotic, chloroform/TFE 1:1 (v/v); LPS model, chloroform/TFE/H_2O (5:5:1); and KDO2, chloroform/methanol/H_2O (90:10:1). These mixtures were plated onto silicon wafers (15 × 30 × 1 mm) via the rock-and-roll method (27) to produce stacks of ∼1800 well-aligned bilayers. After solvent removal under vacuum for 2 h, hydration occurred through the vapor in a thick-walled x-ray hydration chamber (28).

Samples for circular dichroism (CD) spectroscopy were prepared by spreading a thin film of 0.7 mg of the same bacterial mimic mixtures as for x-ray with/without 0.3 mg colistin onto the inner wall of a 1-cm quartz cuvette. After solvent removal under vacuum, CD samples were fully hydrated at room temperature overnight with 100 μL Milli-Q water in the bottom of the sealed cuvette.

Samples for densimetry were prepared as in (29). A quantity of 10–50 mg dried lipid mixture was mixed with ∼1.2 mL water. This mixture was hydrated by temperature cycling three times from 60 to 0°C with vortexing to produce multilamellar vesicles.

Samples for neutron scattering were prepared by adding colistin to 8 mg lipid mixtures in a 50:1 lipid/peptide molar ratio. Organic solvent was removed by evaporation and samples were rehydrated in a 2 M NaCl aqueous solution to a final concentration of 5–6 mg/mL and bath-sonicated for 60–90 min until clarity. The self-assembled monolayers of HC18 tethers were formed on 3" diameter silicon wafers (30) and sparsely tethered bilayer lipid membranes were formed by exposing the self-assembled monolayer to the vesicle suspension for 60 min in a National Institute of Standards and Technology (NIST) reflectivity flow cell. This was followed by a rinse with 40 mL deionized water (31).

Methods

Low-angle x-ray scattering. Low-angle x-ray scattering (LAXS) data from oriented, fully hydrated samples were obtained at the G1 line at the Cornell High Energy Synchrotron Source (CHESS, Ithaca, NY) with previously described methods (32–34) on two separate trips using x-ray wavelengths 1.108 and 1.096 Å and sample-to-detector (S)-distances of 387.2 and 396.6 mm. In addition, a laboratory x-ray source RUH3R Rotating Anode X-Ray Generator (Rigaku, Tokyo, Japan) with a FOX 2D Focusing Collimator (Xenocs, Sassenage, France) and a Mercury CCD Detector (Rigaku) were used with an x-ray wavelength of 1.5418 Å and S-distance of 280.6 mm. Full hydration is judged by no further increase in lamellar D-spacing over time. Measurements were carried out in the fluid phase typically at 37°C, except for KDO2 samples, which were studied at 55°C due to the high melting temperature of the lipid. Details about determination of K_C from diffuse LAXS images and electron density profiles are given in the Supporting Material.

Wide-angle x-ray scattering. Wide-angle x-ray scattering (WAXS) was obtained at CHESS (S-distances = 163.4 and 179.3 mm) and at Carnegie Mellon University (Pittsburgh, PA) (S-distance = 125.7 mm) as described in (29,35). Hydrocarbon chain order parameters were estimated by measuring the angular dependence of the interchain WAXS signal according to the model developed by Mills et al. (35), which is also based upon liquid crystal theory. More details of the WAXS analysis are given in the Supporting Material.

Neutron reflectivity. Neutron reflectivity (NR) measurements were performed at the NGD-MAGIK reflectometer at the NIST Center for Neutron Research (Gaithersburg, MD) over a momentum transfer range 0–0.25 $Å^{-1}$. More details about NR are given in the Supporting Material.

CD spectroscopy. CD spectra in the 200–240-nm range were collected with a model No. 715 Spectropolarimeter (Jasco, Oklahoma City, OK) by accumulating 15 or 20 spectra at 37°C, at 100 nm/min with a step resolution of 1 nm. Samples were performed in duplicate or triplicate. More details of the CD spectroscopy are given in the Supporting Material.

Densimetry. Approximately one milliliter of multilamellar vesicles were loaded into the model No. 5000M Densimeter (Anton-Paar, Graz, Austria). Density measurements were recorded as in (36), by first measuring Milli-Q water at 37°C and then measuring the sample density at 37°C. The sample was withdrawn and remeasured several times to ensure reproducibility. The molecular volume was calculated from density using Avogadro's number and the combined molecular weight of the lipids assuming additivity. Colistin's volume was measured separately as an aqueous solution at 37°C (7.9 mg/mL).

RESULTS

CD

Colistin adopted a secondary structure in water that contained primarily β-sheet, random coil, and β-turn (see Table 1). When associated with lipids in thin films, however, β-turn and β-sheet structure were reduced, and a signal resembling α-helix could be fitted. However, it must be recalled that in peptides, some turns can show the same negative band at 222 nm as a result of n-π* transitions (37,38). What is striking is that colistin's secondary structure is quite similar in all of the lipid models, with slightly higher α-helix-type signal in LPS and eukaryotic membranes. In particular, there is little difference between colistin in G(−) and G(+) membrane mimics. Light microscopy pictures of the thin film samples in the dried state that were then hydrated for CD are shown in Fig. S1. CD ellipticity data that produced the results in Table 1 can be found in Fig. S2.

Diffuse scattering

Fig. S4 shows typical LAXS data from oriented, fully hydrated stacks of membrane mimics containing colistin, 100:1 lipid/colistin. The results of the LAXS fitting are shown in Figs. 1, *A* and *B*, 2, and 3.

Fig. S7 shows WAXS data obtained from the same sample concentrations as in Fig. S4. The results of the WAXS fitting are shown in Fig. 1, *C* and *D*.

TABLE 1 CD Results of Colistin in Water and Membrane Mimics

Colistin Sample	α-Helix-Type %	β-Sheet %	β-Turn %	Random Coil %	R^2
Water	0 ± 1	48 ± 6	16 ± 5	36 ± 8	0.88
G(−)	24 ± 6	18 ± 8	0 ± 1	59 ± 7	0.99
G(+)	17 ± 3	17 ± 4	2 ± 1	64 ± 2	0.99
LPS	31 ± 11	3 ± 3	0 ± 1	67 ± 3	0.99
Eukaryotic	30 ± 10	9 ± 8	0 ± 1	62 ± 12	0.99

Percent composition was obtained by normalizing to 100% the unitless coefficients in the linear least squares fit of the structural motifs to the data. R^2 values indicate goodness of fit, with 1 indicating a perfect fit to the data.

Bending moduli and S_{xray} order parameters

Fig. 1 shows the results of fitting the LAXS (Fig. 1, *A* and *B*) and WAXS (Fig. 1, *C* and *D*) diffuse data for the five lipid membrane mimics containing colistin. Not surprisingly, K_C is highest (stiffest membrane) for the eukaryotic membrane mimic, in which cholesterol interacts favorably with the saturated palmitoyl chain (39) in POPC and POPE (Fig. 1 *A*). Colistin caused only a slight softening of the eukaryotic mimic with increasing concentration. G(+) membrane mimics had a much lower K_C, indicating a more bendable membrane, which was also only slightly softened by colistin. G(−), on the other hand, showed a complex behavior of K_C with colistin concentration. At low (500:1) and high peptide concentration (>100:1 lipid/peptide molar ratio), colistin induced stiffening, but at intermediate ratios (~200:1), a significant membrane softening was obtained (Fig. 1 *A*). For studying the interaction of colistin with the outer membrane of G(−) bacteria, a model mixture consisting of LPS/DLPG (1:3 molar ratio) was employed, because multilayered stacks of pure LPS showed a lamellar x-ray pattern with D-spacing of ~290 Å but no diffuse signal, indicating nonfluctuating bilayers and impairing the analysis of mechanical and structural properties of the membrane within the theoretical framework of liquid crystals. The K_C values in Fig. 1 *B* for LPS/DLPG model were lower than those for the G(+) membrane mimic, indicating that the model used for OM is a relatively soft membrane, whereas DLPG alone (*black triangle*) had a higher K_C, indicating that the additional sugar residues on LPS cause a softening. KDO2 stacked bilayers in fluid phase at 55°C had a higher K_C than LPS/DLPG at 37°C and showed stiffening with increasing colistin content (Fig. 1 *B*). In Fig. 1, *C* and *D*, the complementary S_{xray} results for the K_C results in Fig. 1, *A* and *B* are shown. S_{xray}, which indicates acyl chain order, paralleled membrane bending in all of the membrane mimics. As shown in Fig. 1 *C*, eukaryotic membrane, containing cholesterol, had the most ordered chains, and colistin only slightly disordered them. G(+) had the most disordered chains and colistin slightly disordered them. G(−) showed the same irregular behavior for S_{xray} as for K_C, first increasing chain order at 500:1 lipid/peptide molar ratio, then decreasing chain order at 200:1, then increasing chain order to a maximum at 100:1. In the OM mimics in Fig. 1 *D*, the chain order increased slightly with increasing colistin concentration, similar to the slight membrane stiffening shown in Fig. 1 *B*. Similar to its K_C effect, KDO2 had a higher chain order compared to LPS model. LPS model also has more disordered chains than DLPG, suggesting a chain disordering effect of the sugar residues.

Structural results

Fig. 2 shows the electron density profiles (EDPs) of the five membrane mimics containing the highest concentration in our study of colistin for each mimic. The measured volumes

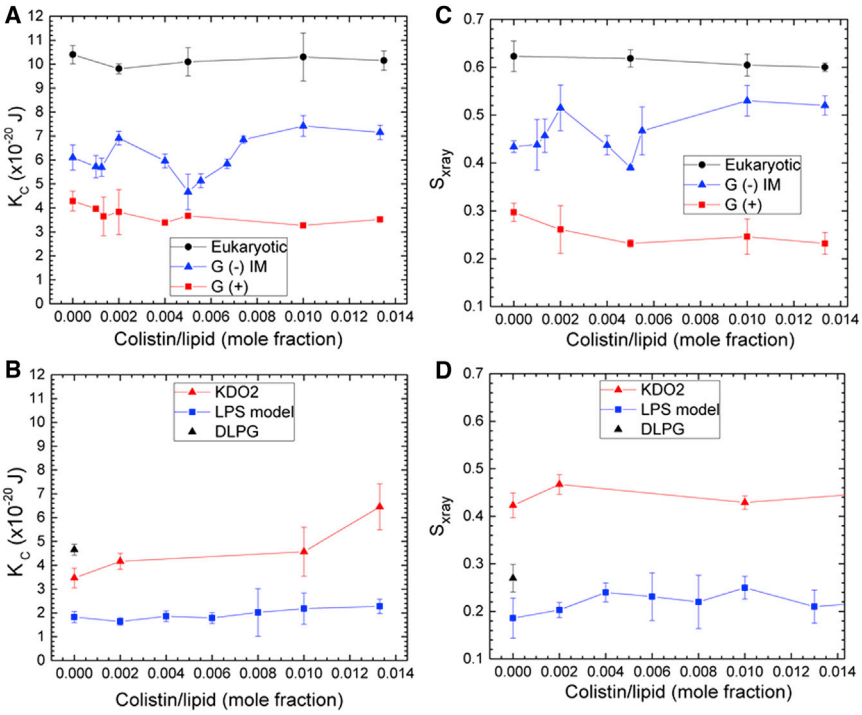

FIGURE 1 Elasticity (K_C) results for (*A*) eukaryotic, G(−) and G(+) membrane mimics, (*B*) KDO2 and LPS model, and DLPG control. S_{xray} order parameter results for (*C*) eukaryotic, G(−) and G(+) membrane mimics, (*D*) KDO2 and LPS model, and DLPG control. To see this figure in color, go online.

required for determining the EDPs appear in Table S1. Colistin (*solid magenta*, Gaussian) showed a deeper partitioning into the G(−) IM membrane mimics (Figs. 2 *C* and 3 *C*) when compared to both G(+) and eukaryotic mimics at the different lipid/peptide mole ratios assayed. In G(−) IM, colistin is located in the hydrocarbon region just within the interfacial region, 11–14 Å from the bilayer center, at all concentrations. In eukaryotic and G(+) membrane, colistin locates in the headgroup region, just within $D_{HH}/2$. Colistin in G(−) mimics locates in the headgroup region in KDO2 (Fig. 2 *A*) and outside of the headgroup maximum ($D_{HH}/2$) in the mixture LPS/DLPG (1:3) (Fig. 2 *B*). The EDP of the LPS/DLPG mixture was calculated taking into account the electrons from the Re variant of the LPS molecule (lipid A plus the inner sugar core, consisting of three residues of deoxy-manno-octulosonyl and 2 phospho-heptose), whereas the remainder sugar moieties in the core and O-antigen regions were included in the water electron density.

Fig. 3 summarizes the structural results for all five membrane mimics with increasing colistin concentration. A_L is the area/unit cell, which includes the lipid and the colistin, but not the cholesterol (for eukaryotic membrane). In G(−) IM, A_L (*black lines*) decreased at 500:1 lipid/peptide molar ratio but increased at 200:1. These changes are in the expected direction according to the S_{xray} results in Fig. 1 *C*, because increasing chain order decreases A_L, as the chains straighten. At peptide concentrations higher than 100:1, A_L showed no significant differences when compared to control. The overall bilayer thickness ($D_{HH}/2$, *red lines*) did not change appreciably. In G(+) membranes, A_L first decreases slightly then increases with colistin concentration, whereas in eukaryotic membranes, there is an increase in A_L with colistin concentration. A_L is fairly constant as colistin is added to KDO2 and LPS model, as is the bilayer thickness, $D_{HH}/2$. Table S4 compares our KDO2 control area with literature values.

NR

Fig. 4 shows the NR results as component volume occupancy versus distance from the gold substrate. At this concentration of lipid/peptide (50:1), colistin (*red line*) enters more deeply into the G(−) membrane (Fig. 4 *A*) than into the G(+) membrane (Fig. 4 *B*). However, compared to the x-ray result, there is considerable colistin outside of the outer leaflet headgroup Gaussian (*cyan*) for both G(−) and G(+) membrane mimics. This could be due to the different sample preparation using vesicle fusion to form a single tethered bilayer, compared to the stacked system of 1800 bilayers for x-ray. The significance of the NR result is that there is a deeper penetration of colistin into the hydrocarbon core in G(−) membrane mimics, similar to the x-ray result. Additional details of the NR results are shown in the Supporting Material.

DISCUSSION

Colistin secondary structure is similar in different membrane mimics

A shape analysis procedure (38) for fitting the experimental CD spectra was undertaken for estimating the secondary

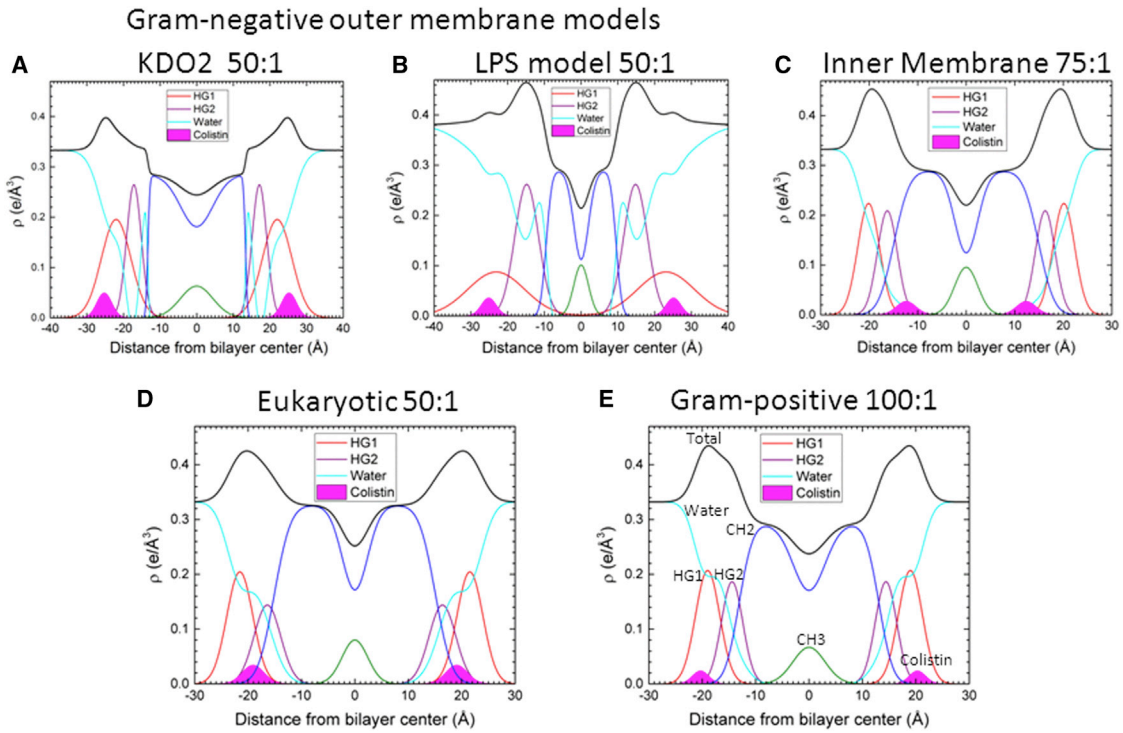

FIGURE 2 EDPs for (*A*) KDO2, 50:1 lipid/peptide molar ratio; (*B*) LPS model, 50:1; (*C*) IM, 75:1; (*D*) Eukaryotic, 50:1; (*E*) G(+), 100:1. Component groups are headgroup HG1 (*red*), headgroup HG2 (*violet*), methylene CH2 region (*blue*), methyl CH3 region (*green*), colistin (*solid magenta*), water (*cyan*), and total (*black*). To see this figure in color, go online.

structure of colistin, using a set of spectra of typical motifs obtained from standard proteins/polypeptides (40). Although these reference spectra correspond to proteins formed by the naturally occurring L isomer of amino acids, we employed them for this colistin analysis, whose primary structure is formed of nine L-amino acids plus one D-amino acid. This method was appropriate because several previous reports indicated that CD is a sensitive measurement of the secondary structural changes caused by single or double D-amino acid substitution in short peptides (41–43). On the other hand, complete inverse CD structure is obtained in an all-D model α-helixes (44,45). Our study indicates that, in agreement with previous NMR results (46,47), the colistin backbone in the aqueous phase has a significant degree of freedom, with a high random coil or disordered structure plus β-turn and β-sheet. When bound to lipids, both β-turn and β-sheet content decreased whereas disordered structure increased, which agrees with the weakening of the β-turn NMR signal observed previously (46). However, the α-helix-type feature was also found, which could be ascribed to distorted turns, as previously observed for other cyclic peptides and D-amino acid-containing peptides (43).

The further result that there were no significant differences in secondary structure of colistin when bound to the different membrane mimics, suggests that a change in colistin secondary structure cannot be the reason for differences in bactericidal mechanism in G(−) versus G(+) bacteria.

Colistin's effects on G(−) IM membrane mechanical properties and order parameters may involve lateral heterogeneity

Contrary to the CD results, dramatic changes were observed in the elastic behavior of colistin interacting with G(−) IM mimics compared to G(+) mimics. As shown in Fig. 1 *A*, colistin caused alternating stiffening, softening and stiffening, as its concentration increased in G(−) IM mimics. This erratic behavior was mirrored by the S_{xray} order parameter (Fig. 1 *C*), where colistin alternately ordered, disordered and ordered the acyl chains at the same concentrations as for K_C. These changes are unlike any seen in our previous investigations: increasing concentration of HIV-1 fusion peptide (48) or alamethicin (49) decreased the bending modulus K_C in DOPC and diC22:1PC in an exponential fashion, and increasing HIV-1 matrix$_{31}$ peptide caused a gradual increase in K_C and S_{xray} then a gradual decrease in both in PS-containing membranes (29). The fact that this sharply irregular behavior occurred only in G(−) IM mimics may offer a clue to colistin's bactericidal mechanism in G(−) bacteria. Compared to G(+) mimics, which displayed only a slight softening and disordering of lipid chains, G(−) IM mimics were greatly perturbed, in both directions, by colistin.

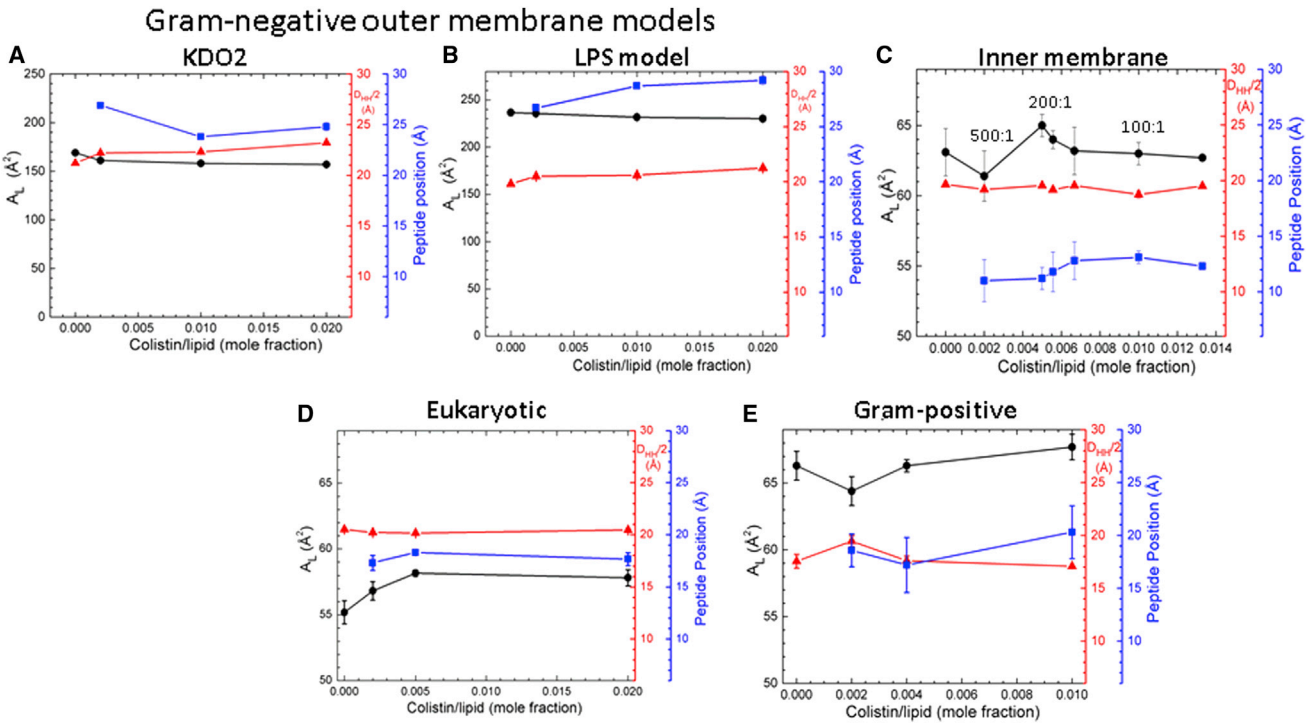

FIGURE 3 Structural parameters, area/lipid A_L (*black lines*), $D_{HH}/2$ (*red lines*) and colistin position (*blue lines*), as a function of increasing colistin mole fraction in five lipid membrane mimics: (*A*) KDO2, (*B*) LPS model, (*C*) G(−) IM, (*D*) Eukaryotic, and (*E*) G(+). Left axis shows A_L (*black*); right axes show $D_{HH}/2$ (*red*) and peptide position (*blue*). $D_{HH}/2$ and peptide position are in Å units from the bilayer center, and A_L is in units of Å^2. To see this figure in color, go online.

The G(+) mimic used in this work consisted of the lipid mixture POPG/DOTAP/POPE/TOCL (6:1.5:1.5:1 molar ratio), as many Gram-positive bacteria, such as *Staphylococcus aureus*, contain a high amount of the negatively charged lipids PG and cardiolipin, but also a positively charged derivative of PG, lysyl-PG, in which a lysine residue is bonded to the PG headgroup (50). Due to the high amounts of lipids needed for preparing samples in a wide range of peptide concentrations, a more affordable lipid, DOTAP, was used instead of lysyl-PG, which is also positively charged. A control sample prepared with lysyl-PG showed no significant differences in A_L or K_C compared to mixtures prepared with DOTAP, indicating that the latter is a good surrogate for lysyl-PG. Unlike G(+) membranes, the inner membranes of G(−) bacteria are highly enriched in PE but also contain a significant amount of negatively charged lipids (51,52), so this mimic contained POPE/POPG/TOCL (7:2:1).

It has been suggested that cardiolipin-rich domains exist in G(−) membranes (53) and similar cationic antimicrobial peptides can perturb bilayer permeability by inducing phase separation in membranes containing PE and cardiolipin (54). Thus, we propose that colistin may induce membrane lateral heterogeneity by clustering anionic lipids due to Coulombic interactions in the presence of high content of PE, as in IM G(−) membranes but not in a low content of PE, as in G(+) membranes. Formation of lipid domains can lead to interfacial curvature stress in bilayers, due to a nonbilayer tendency that some of them have, like PE (55) or cardiolipin (56). A previous work found that the increase

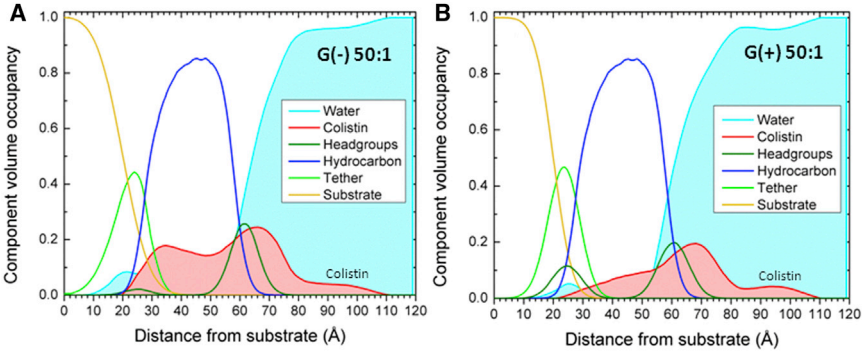

FIGURE 4 Component volume occupancy versus distance from substrate. (*A*) G(−) IM mimic; (*B*) G(+) mimic. Lipid/peptide 50:1 molar ratio. Component groups are shown: water (*cyan*), colistin (*red*), headgroups (*olive*), hydrocarbons (*blue*), tether (*green*), and substrate (*gold*). To see this figure in color, go online.

in current due to permeability perturbation in asymmetric model membranes occurred above a threshold colistin concentration, which was also postulated to be a consequence of preferential binding of the peptide with negatively charged lipids and phase separation (57). The presence of lipid domains and interfacial curvature stress would explain transient membrane permeabilization along the defects at domain boundaries (54). In a recent molecular dynamics (MD) simulation (58), it was shown that the bending modulus was altered as a cationic AMP was added to a binary lipid membrane containing the zwitterionic DPPC and the negatively charged DPPS. The authors suggested that when cationic AMPs encounter bacterial membranes, domains with different material moduli are formed, which could lead to a destabilization at the boundaries of these domains. To investigate this possibility further, we have studied the K_C values of the individual components of G(−) IM, with and without 0.01 mol fraction colistin, with results shown in Table 2. K_C of POPG is reduced by about half when colistin is added, whereas K_C of TOCL is only slightly reduced. POPE with 0.01 colistin, or even 0.001 colistin, did not fluctuate, indicating that K_C has been greatly increased by colistin (i.e., membrane is stiffer). Thus, even though PE is the lipid at highest proportion in G(−) IM, the softening of the mixture at intermediate colistin mole fractions should be produced by a preferential interaction of colistin with PG or TOCL due to Coulombic forces, whereas the stiffening caused by colistin-PE interaction is evidenced at intermediate and higher concentrations. When these results are compared to Fig. 1 *A*, we might interpret the initial slight lowering of K_C as due to colistin binding to TOCL. As concentration increases, colistin could bind to POPE, thus increasing K_C. When colistin encounters POPG, a larger decrease in K_C is observed. At the highest concentrations, colistin interacts with the remaining POPE, causing a final increase in K_C. A cartoon summarizing this scenario is presented in Fig. 5.

A second reason for differences between G(+) and G(−) IM is that colistin reaches the deepest location in the hydrocarbon region in G(−) IM when compared to the other membrane mimics. The EDPs and summary of structural results show that colistin is located in the headgroup region at all concentrations for all mimics except for G(−) IM. NR supports this location, although the contrast between G(−) and G(+) is not as dramatic as in x-ray, presumably due to the different sample preparations. This deeper location of colistin in G(−) IM could cause a defect that would allow for a deeper penetration of water into the bilayer, leading to permeabilization and bacterial cell death.

TABLE 2 Bending Moduli, K_C Values, of Components of G(−) Inner Membranes

Colistin Mole Fraction	POPE	POPG	TOCL
0	9.7 ± 1.0	7.5 ± 0.3	4.4 ± 0.4
0.01	ND	3.7 ± 0.4	3.3 ± 1.0

K_c units ($\times 10^{-20}$ J). ND, none detected.

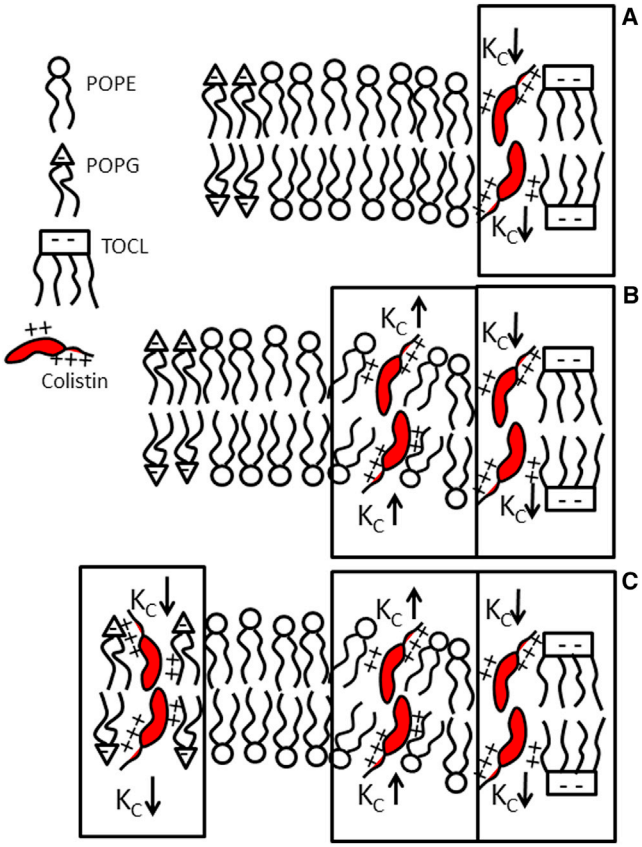

FIGURE 5 Cartoon showing colistin interacting with individual lipid types in G(−) IM as its concentration increases. (*A*) By comparing to Fig. 1 *A*, colistin may first interact with TOCL, slightly lowering K_C. (*B*) Colistin may then interact with POPE, increasing K_C. (*C*) Colistin may then interact with POPG, decreasing K_C substantially. Finally, colistin may interact with the remaining POPE (data not shown), causing an increase in K_C. To see this figure in color, go online.

Colistin locates in the headgroup region in G(−) OM mimics

As for the G(−) OM mimics, we observe that the LPS model (LPS/DLPG 1:3) is softer and less ordered than DLPG or KDO2, indicating that the LPS component with its core and O-antigen sugar residues induces a softening and disordering effect. This contradicts the idea that the OM has low fluidity (59,60), but is in agreement with order parameters calculated by MD simulation that showed $|S_{CD}|$ decreases with increasing sugar residues on lipid A (61). The hydrocarbon half-thickness for the two OM control mimics (EDPs not shown) are both thinner than usual (D_C = 12.2 Å for KDO2 and 9.2 Å for LPS model), whereas the other control mimics have more normal thicknesses (D_C = 14.4 Å for G(+), 14.8 Å for G(−), and 15.4 Å for eukaryotic). We find that colistin slightly orders both KDO2 and

the LPS model, contradicting the Fourier transform infrared spectroscopy results of (62), which showed a fluidizing effect of the related polymyxin B on KDO2. However, in that study, the smallest concentration of lipid/peptide was 8:1, a much larger amount of colistin than in our study. The small effect of colistin in our model OM systems agrees with previous results with polymyxin B, in which lower charge screening and permeabilization are observed in LPS- compared to PG-containing lipid vesicles (63).

Colistin's location in the headgroup of KDO2 and the LPS model suggests that the outer membrane destabilization observed in previous biophysical and microbiological works must occur through divalent cation displacement by colistin (18,64). Although our study did not add Ca^{2+} or Mg^{2+} as variables, our main conclusion, that colistin remains in the headgroup region of G(−) OM models, is consistent with the idea that it could displace divalent cations. Future experiments could explore the dependence of colistin's location on type of divalent cation. The divalent cations play an important role in the assembly of the LPS molecules in the outer membrane by screening the repulsive Coulombic forces between the phosphate residues at the lipid A and sugar inner core levels (59). It was previously reported that colistin binding to lipid A is inhibited by divalent cations and high ionic strength (64). By weakening the outer membrane, colistin could induce its self-promoted uptake toward the periplasmic space and reach its final target, the inner membrane of G(−) bacteria. A recent MD simulation confirmed our headgroup location of colistin in KDO2 and the LPS model (65).

CONCLUSIONS

Using a structural and materials approach, this work attempted to clarify molecular steps in colistin's bactericidal mechanism. We found no difference in secondary structure of colistin in G(−) IM and G(+) membranes, thus ruling out a protein conformational change as the cause of colistin's ability to kill G(−) but not G(+) bacteria. However, dramatic differences between colistin's effect on G(−) IM versus G(+) membrane mimics were observed in the elasticity results; whereas G(−) IM mimics were softened at a critical lipid/peptide molar ratio (200:1), they were stiffened above and below that ratio. G(+) membranes, on the other hand, were only slightly softened, a very small perturbation. We suggest that colistin induces domains in G(−) IM with different adjacent elasticity, which could lead to permeation through the domain boundaries. Chain ordering paralleled membrane elasticity to indicate that lipid acyl chains are significantly perturbed only in the case of G(−) IM. In addition, colistin located at a deepest position in the interior of the hydrocarbon region in G(−) membranes. Therefore, the elasticity, chain ordering, and peptide membrane location point to colistin's ability to enter into and perturb the G(−) inner membrane, which could lead to an increase in permeability. As for the G(−) OM, colistin remains in the headgroup region at all the concentrations that we studied, and increases slightly the OM stiffness and chain order. Therefore, colistin is in position to displace divalent cations, leading to OM perturbation, and eventually, to its self-promoted uptake.

SUPPORTING MATERIAL

Supporting Materials and Methods, ten figures, and four tables are available at http://www.biophysj.org/biophysj/supplemental/S0006-3495(17)35132-9.

AUTHOR CONTRIBUTIONS

F.G.D. and S.T.-N. designed the experimental research, performed experiments, analyzed data, and wrote the manuscript. I.P., K.A., and F.H. performed experiments and analyzed data. M.F.P. and Y.E. performed experiments.

ACKNOWLEDGMENTS

The authors thank Prof. Emeritus John F. Nagle for help with the data collection at CHESS and for discussions concerning the use of the SDP program, and Dr. Yohei Doi for critical reading of the manuscript and Dr. Arthur Woll for his help at the G1 CHESS beamline.

Parts of this research were performed at the NIST Center for Nanoscale Science. Certain commercial materials, equipment, and instruments are identified in this work to describe the experimental procedure as completely as possible. In no case does such an identification imply a recommendation or endorsement by NIST, nor does it imply that the materials, equipment, or instrument identified are necessarily the best available for the purpose.

Support for this work was from the Samuel and Emma Winters Foundation (STN), The National Scientific and Technical Research Council, Argentina (CONICET) under Programa de Becas Externas (to F.G.D.), The National Scientific and Technical Research Council, Argentina (CONICET) (MFP), and National Institutes of Health (NIH) R01GM101647 (to F.H.). This work is based upon research conducted at Carnegie Mellon University and at the Cornell High Energy Synchrotron Source (CHESS), which is supported by the National Science Foundation (NSF) under award No. DMR-1332208. The neutron work was supported by the Department of Commerce through its Measurement Science and Engineering Program (70NANB13H009), the National Institute of Standards and Technology (NIST) Center for Neutron Research Comprehensive Grant Program (70NANB17H299), and the NIST IMS Program "Precision Measurement for Integral Membrane Proteins".

SUPPORTING CITATIONS

References (66–79) appear in the Supporting Material.

REFERENCES

1. Koyama, Y., A. Kurosawa, …, K. Takakuta. 1950. A new antibiotic 'colistin' produced by spore-forming soil bacteria. *J. Antibiotics (Japan).* 3:457–458.
2. Stein, T., J. Vater, …, H. R. Morris. 1996. The multiple carrier model of nonribosomal peptide biosynthesis at modular multienzymatic templates. *J. Biol. Chem.* 271:15428–15435.
3. Velkov, T., K. D. Roberts, …, J. Li. 2013. Pharmacology of polymyxins: new insights into an 'old' class of antibiotics. *Future Microbiol.* 8:711–724.
4. Li, J., R. L. Nation, …, D. L. Paterson. 2006. Colistin: the re-emerging antibiotic for multidrug-resistant Gram-negative bacterial infections. *Lancet Infect. Dis.* 6:589–601.

5. Bergen, P. J., C. B. Landersdorfer, …, J. Li. 2012. Pharmacokinetics and pharmacodynamics of 'old' polymyxins: what is new? *Diagn. Microbiol. Infect. Dis.* 74:213–223.
6. Infectious Diseases Society of America.. 2010. The 10 × 20 initiative: pursuing a global commitment to develop 10 new antibacterial drugs by 2020. *Clin. Infect. Dis.* 50:1081–1083.
7. Talbot, G. H., J. Bradley, …, J. G. Bartlett; Antimicrobial Availability Task Force of the Infectious Diseases Society of America. 2006. Bad bugs need drugs: an update on the development pipeline from the Antimicrobial Availability Task Force of the Infectious Diseases Society of America. *Clin. Infect. Dis.* 42:657–668.
8. Gales, A. C., R. N. Jones, and H. S. Sader. 2011. Contemporary activity of colistin and polymyxin B against a worldwide collection of Gram-negative pathogens: results from the SENTRY antimicrobial surveillance program (2006–09). *J. Antimicrob. Chemother.* 66:2070–2074.
9. Bergen, P. J., J. Li, …, R. W. Milne. 2008. Comparison of once-, twice-, and thrice-daily dosing of colistin on antibacterial effect and emergence of resistance: studies with *Pseudomonas aeruginosa* in an in vitro pharmacodynamic model. *J. Antimicrob. Chemother.* 61: 636–642.
10. Poudyal, A., B. P. Howden, …, J. Li. 2008. In vitro pharmacodynamics of colistin against multidrug-resistant *Klebsiella pneumoniae*. *J. Antimicrob. Chemother.* 62:1311–1318.
11. McGann, P., E. Snesrud, …, K. E. Schaecher. 2016. *Escherichia coli* harboring mcr-1 and blaCTX-M on a novel IncF plasmid: first report of MCR-1 in the United States. *Antimicrob. Agents Chemother.* 60:4420–4421.
12. Qureshi, Z. A., L. E. Hittle, …, Y. Doi. 2015. Colistin-resistant *Acinetobacter baumannii*: beyond carbapenem resistance. *Clin. Infect. Dis.* 60:1295–1303.
13. Matthaiou, D. K., A. Michalopoulos, …, M. E. Falagas. 2008. Risk factors associated with the isolation of colistin-resistant Gram-negative bacteria: a matched case-control study. *Crit. Care Med.* 36:807–811.
14. Liu, Y. Y., Y. Wang, …, J. Shen. 2016. Emergence of plasmid-mediated colistin resistance mechanism MCR-1 in animals and human beings in China: a microbiological and molecular biological study. *Lancet Infect. Dis.* 16:161–168.
15. Morrison, D. C., and D. M. Jacobs. 1976. Binding of polymyxin B to the lipid A portion of bacterial lipopolysaccharides. *Immunochemistry.* 13:813–818.
16. Cai, Y., D. Chai, …, N. Bai. 2012. Colistin resistance of *Acinetobacter baumannii*: clinical reports, mechanisms and antimicrobial strategies. *J. Antimicrob. Chemother.* 67:1607–1615.
17. Koike, M., K. Iida, and T. Matsuo. 1969. Electron microscopic studies on mode of action of polymyxin. *J. Bacteriol.* 97:448–452.
18. Zhang, L., P. Dhillon, …, R. E. Hancock. 2000. Interactions of bacterial cationic peptide antibiotics with outer and cytoplasmic membranes of *Pseudomonas aeruginosa*. *Antimicrob. Agents Chemother.* 44:3317–3321.
19. Hancock, R. E. W. 1984. Alterations in outer membrane permeability. *Annu. Rev. Microbiol.* 38:237–264.
20. Hancock, R. E., V. J. Raffle, and T. I. Nicas. 1981. Involvement of the outer membrane in gentamicin and streptomycin uptake and killing in *Pseudomonas aeruginosa*. *Antimicrob. Agents Chemother.* 19:777–785.
21. Hancock, R. E. W., and D. S. Chapple. 1999. Peptide antibiotics. *Antimicrob. Agents Chemother.* 43:1317–1323.
22. Hancock, R. E. W. 1997. Peptide antibiotics. *Lancet.* 349:418–422.
23. Hancock, R. E. W., T. Falla, and M. Brown. 1995. Cationic bactericidal peptides. *Adv. Microb. Physiol.* 37:135–175.
24. Clausell, A., M. Garcia-Subirats, …, Y. Cajal. 2007. Gram-negative outer and inner membrane models: insertion of cyclic cationic lipopeptides. *J. Phys. Chem. B.* 111:551–563.
25. Cajal, Y., J. Rogers, …, M. K. Jain. 1996. Intermembrane molecular contacts by polymyxin B mediate exchange of phospholipids. *Biochemistry.* 35:299–308.
26. Kohanski, M. A., D. J. Dwyer, …, J. J. Collins. 2007. A common mechanism of cellular death induced by bactericidal antibiotics. *Cell.* 130:797–810.
27. Tristram-Nagle, S. 2007. Preparation of Oriented, Fully Hydrated Lipid Samples for Structure Determination Using X-Ray Scattering. Humana Press, Totowa, NJ.
28. Kucerka, N., Y. Liu, …, J. F. Nagle. 2005. Structure of fully hydrated fluid phase DMPC and DLPC lipid bilayers using x-ray scattering from oriented multilamellar arrays and from unilamellar vesicles. *Biophys. J.* 88:2626–2637.
29. O'Neil, L., K. Andenoro, …, S. Tristram-Nagle. 2016. HIV-1 matrix-31 membrane binding peptide interacts differently with membranes containing PS vs. PI(4,5)P2. *Biochim. Biophys. Acta.* 1858:3071–3081.
30. Budvytyte, R., G. Valincius, …, D. J. Vanderah. 2013. Structure and properties of tethered bilayer lipid membranes with unsaturated anchor molecules. *Langmuir.* 29:8645–8656.
31. Barros, M., F. Heinrich, …, M. Lösche. 2016. Membrane binding of HIV-1 matrix protein: dependence on bilayer composition and protein lipidation. *J. Virol.* 90:4544–4555.
32. Liu, Y., and J. F. Nagle. 2004. Diffuse scattering provides material parameters and electron density profiles of biomembranes. *Phys. Rev. E Stat. Nonlin. Soft Matter Phys.* 69:040901.
33. Lyatskaya, Y., Y. Liu, …, J. F. Nagle. 2001. Method for obtaining structure and interactions from oriented lipid bilayers. *Phys. Rev. E Stat. Nonlin. Soft Matter Phys.* 63:011907.
34. Liu, Y. 2003. New method to obtain structure of biomembranes using diffuse x-ray scattering: application to fluid phase DOPC lipid bilayers. Ph.D. thesis. Carnegie Mellon University, Pittsburgh, PA.
35. Mills, T. T., G. E. S. Toombes, …, J. F. Nagle. 2008. Order parameters and areas in fluid-phase oriented lipid membranes using wide angle x-ray scattering. *Biophys. J.* 95:669–681.
36. Boscia, A. L., K. Akabori, …, S. Tristram-Nagle. 2013. Membrane structure correlates to function of LLP2 on the cytoplasmic tail of HIV-1 gp41 protein. *Biophys. J.* 105:657–666.
37. Adler, A. J., N. J. Greenfield, and G. D. Fasman. 1973. Circular dichroism and optical rotatory dispersion of proteins and polypeptides. *Methods Enzymol.* 27:675–735.
38. Greenfield, N. J. 2006. Using circular dichroism spectra to estimate protein secondary structure. *Nat. Protoc.* 1:2876–2890.
39. Pan, J., T. T. Mills, …, J. F. Nagle. 2008. Cholesterol perturbs lipid bilayers nonuniversally. *Phys. Rev. Lett.* 100:198103.
40. Brahms, S., and J. Brahms. 1980. Determination of protein secondary structure in solution by vacuum ultraviolet circular dichroism. *J. Mol. Biol.* 138:149–178.
41. Rothemund, S., M. Beyermann, …, F. D. Sönnichsen. 1995. Structure effects of double D-amino acid replacements: a nuclear magnetic resonance and circular dichroism study using amphipathic model helices. *Biochemistry.* 34:12954–12962.
42. Krause, E., M. Beyermann, …, M. Bienert. 1996. Conformation of a water-soluble β-sheet model peptide. A circular dichroism and Fourier-transform infrared spectroscopic study of double D-amino acid replacements. *Int. J. Pept. Protein Res.* 48:559–568.
43. Lee, D. L., J. P. Powers, …, R. S. Hodges. 2004. Effects of single D-amino acid substitutions on disruption of β-sheet structure and hydrophobicity in cyclic 14-residue antimicrobial peptide analogs related to gramicidin S. *J. Pept. Res.* 63:69–84.
44. Scolnik, Y., I. Portnaya, …, M. Shinitzky. 2006. Subtle differences in structural transitions between poly-L- and poly-D-amino acids of equal length in water. *Phys. Chem. Chem. Phys.* 8:333–339.
45. Wade, D., A. Boman, …, R. B. Merrifield. 1990. All-D amino acid-containing channel-forming antibiotic peptides. *Proc. Natl. Acad. Sci. USA.* 87:4761–4765.
46. Pristovsek, P., and J. Kidric. 1999. Solution structure of polymyxins B and E and effect of binding to lipopolysaccharide: an NMR and molecular modeling study. *J. Med. Chem.* 42:4604–4613.

47. Bhattacharjya, S., S. A. David, …, P. Balaram. 1997. Polymyxin B nonapeptide: conformations in water and in the lipopolysaccharide-bound state determined by two-dimensional NMR and molecular dynamics. *Biopolymers.* 41:251–265.

48. Tristram-Nagle, S., and J. F. Nagle. 2007. HIV-1 fusion peptide decreases bending energy and promotes curved fusion intermediates. *Biophys. J.* 93:2048–2055.

49. Pan, J., D. P. Tieleman, …, S. Tristram-Nagle. 2009. Alamethicin in lipid bilayers: combined use of x-ray scattering and MD simulations. *Biochim. Biophys. Acta.* 1788:1387–1397.

50. O'Leary, W. M., and S. G. Wilkinson. 1989. Microbial Lipids C. Ratledge, and S. G. Wilkinson, eds. Academic Press, San Diego, CA.

51. O'Leary, W. M., and S. G. Wilkinson. 1989. Microbial Lipids C. Ratledge, and S. G. Wilkinson, eds. Academic Press, San Diego, CA.

52. F. H. Neidhardt, ed 1996. *Escherichia coli* and *Salmonella*: Cellular and Molecular BiologyVol. 1. ASM Press, Washington, DC.

53. Mileykovskaya, E., and W. Dowhan. 2000. Visualization of phospholipid domains in *Escherichia coli* by using the cardiolipin-specific fluorescent dye 10-N-nonyl acridine orange. *J. Bacteriol.* 182:1172–1175.

54. Epand, R. M., S. Rotem, …, R. F. Epand. 2008. Bacterial membranes as predictors of antimicrobial potency. *J. Am. Chem. Soc.* 130:14346–14352.

55. Seddon, J. M. 1990. Structure of the inverted hexagonal (HII) phase, and non-lamellar phase transitions of lipids. *Biochim. Biophys. Acta.* 1031:1–69.

56. Bergstrom, C. L., P. A. Beales, …, J. T. Groves. 2013. Cytochrome *c* causes pore formation in cardiolipin-containing membranes. *Proc. Natl. Acad. Sci. USA.* 110:6269–6274.

57. Schröder, G., K. Brandenburg, and U. Seydel. 1992. Polymyxin B induces transient permeability fluctuations in asymmetric planar lipopolysaccharide/phospholipid bilayers. *Biochemistry.* 31:631–638.

58. Lopez Cascales, J. J., A. Garro, …, R. D. Enriz. 2014. The dynamic action mechanism of small cationic antimicrobial peptides. *Phys. Chem. Chem. Phys.* 16:21694–21705.

59. F. H. Neidhardt, ed 1996. *Escherichia coli* and *Salmonella*: Cellular and Molecular BiologyVol. 2. ASM Press, Washington, DC.

60. Labischinski, H., G. Barnickel, …, P. Giesbrecht. 1985. High state of order of isolated bacterial lipopolysaccharide and its possible contribution to the permeation barrier property of the outer membrane. *J. Bacteriol.* 162:9–20.

61. Wu, E. L., O. Engström, …, W. Im. 2013. Molecular dynamics and NMR spectroscopy studies of *E. coli* lipopolysaccharide structure and dynamics. *Biophys. J.* 105:1444–1455.

62. Brandenburg, K., I. Moriyon, …, U. Seydel. 2002. Biophysical investigations into the interaction of lipopolysaccharide with polymyxins. *Thermochim. Acta.* 382:189–198.

63. Domingues, M. M., R. G. Inácio, …, N. C. Santos. 2012. Biophysical characterization of polymyxin B interaction with LPS aggregates and membrane model systems. *Biopolymers.* 98:338–344.

64. Schindler, M., and M. J. Osborn. 1979. Interaction of divalent cations and polymyxin B with lipopolysaccharide. *Biochemistry.* 18:4425–4430.

65. Berglund, N. A., T. J. Piggot, …, S. Khalid. 2015. Interaction of the antimicrobial peptide polymyxin B1 with both membranes of *E. coli*: a molecular dynamics study. *PLoS Comput. Biol.* 11:e1004180.

66. Brahms, S., J. Brahms, …, A. Brack. 1977. Identification of β, β-turns and unordered conformations in polypeptide chains by vacuum ultraviolet circular dichroism. *Proc. Natl. Acad. Sci. USA.* 74:3208–3212.

67. Reed, J., and T. A. Reed. 1997. A set of constructed type spectra for the practical estimation of peptide secondary structure from circular dichroism. *Anal. Biochem.* 254:36–40.

68. Tristram-Nagle, S., and J. F. Nagle. 2004. Lipid bilayers: thermodynamics, structure, fluctuations, and interactions. *Chem. Phys. Lipids.* 127:3–14.

69. Kucerka, N., J. F. Nagle, …, J. Katsaras. 2008. Lipid bilayer structure determined by the simultaneous analysis of neutron and x-ray scattering data. *Biophys. J.* 95:2356–2367.

70. Tristram-Nagle, S., Y. Liu, …, J. F. Nagle. 2002. Structure of gel phase DMPC determined by x-ray diffraction. *Biophys. J.* 83:3324–3335.

71. Nagle, J. F., and S. Tristram-Nagle. 2000. Structure of lipid bilayers. *Biochim. Biophys. Acta.* 1469:159–195.

72. Boscia, A. L., B. W. Treece, …, S. Tristram-Nagle. 2014. X-ray structure, thermodynamics, elastic properties and MD simulations of cardiolipin/dimyristoylphosphatidylcholine mixed membranes. *Chem. Phys. Lipids.* 178:1–10.

73. Murzyn, K., and M. Pasenkiewicz-Gierula. 2015. Structural properties of the water/membrane interface of a bilayer built of the *E. coli* lipid A. *J. Phys. Chem. B.* 119:5846–5856.

74. Molecular Modeling Pro. 2017. Norgwyn Montgomery Software, Inc. (NGMSI), North Wales, PA. http://www.norgwyn.com/mmpplus.html.

75. Mills, T. T., S. Tristram-Nagle, …, G. W. Feigenson. 2008. Liquid-liquid domains in bilayers detected by wide angle x-ray scattering. *Biophys. J.* 95:682–690.

76. McGillivray, D. J., G. Valincius, …, M. Lösche. 2007. Molecular-scale structural and functional characterization of sparsely tethered bilayer lipid membranes. *Biointerphases.* 2:21–33.

77. Heinrich, F., and M. Lösche. 2014. Zooming in on disordered systems: neutron reflection studies of proteins associated with fluid membranes. *Biochim. Biophys. Acta.* 1838:2341–2349.

78. Snyder, S., D. Kim, and T. J. McIntosh. 1999. Lipopolysaccharide bilayer structure: effect of chemotype, core mutations, divalent cations, and temperature. *Biochemistry.* 38:10758–10767.

79. Soares, T. A., and T. P. Straatsma. 2008. Assessment of the convergence of molecular dynamics simulations of lipopolysaccharide membranes. *Mol. Simul.* 34:295–307.

Biophysical Journal, Volume *114*

Supplemental Information

Selective Interaction of Colistin with Lipid Model Membranes

Fernando G. Dupuy, Isabella Pagano, Kathryn Andenoro, Maria F. Peralta, Yasmene Elhady, Frank Heinrich, and Stephanie Tristram-Nagle

SUPPORTING MATERIAL for

Selective interaction of colistin with lipid model membranes

Fernando G. Dupuy[1,2], Isabella Pagano[1], Kathryn Andenoro[1], Maria F. Peralta[1,3], Yasmene Elhady[1], Frank Heinrich[1,4] and Stephanie Tristram-Nagle[1]

[1]*Biological Physics Group, Physics Department, Carnegie Mellon University, Pittsburgh, PA 15213*
[2]*Instituto de Química Biológica, National University of Tucumán, San Miguel de Tucumán, Argentina*
[3]*Instituto de Investigación Médica M y M Ferreyra, CONICET-National University of Córdoba, Córdoba, Argentina*
[4]*National Institute of Standards and Technology Center for Neutron Research, Gaithersburg, MD 20899*

1. Details of CD spectroscopy

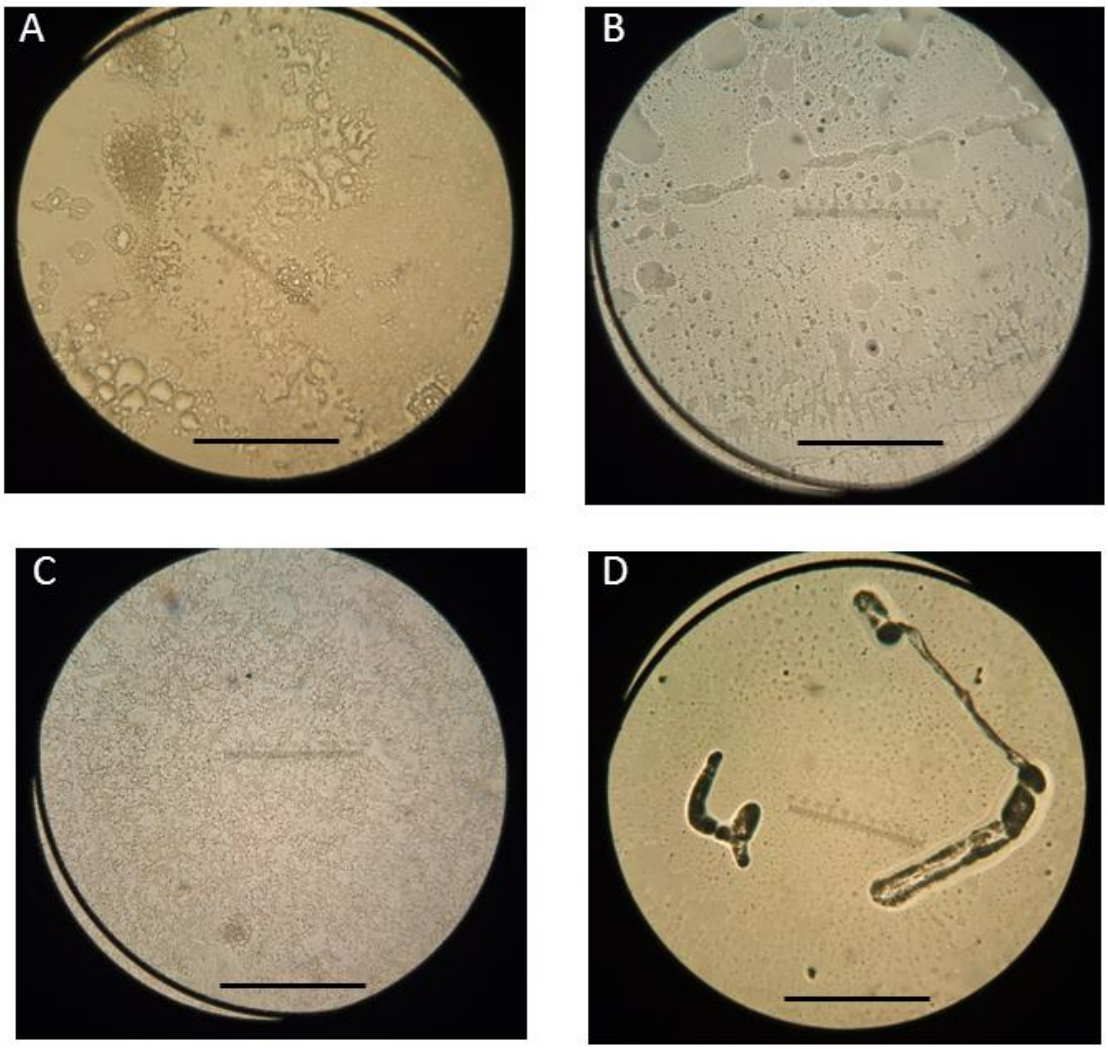

Figure S1. Light microscopy images of thin lipid films on the inner wall of a CD quartz cuvette before hydration. Samples contained colistin mixed with lipid mimics. As shown, samples were not well oriented (homogeneous) and colistin sometimes crystallized out. A. LPS model/colistin, B. G(+) mimic/colistin C. G(-) mimic/colistin D. Eukaryotic (Euk) mimic/colistin. Scale bar represents 500 microns.

Circular Dichroism Results

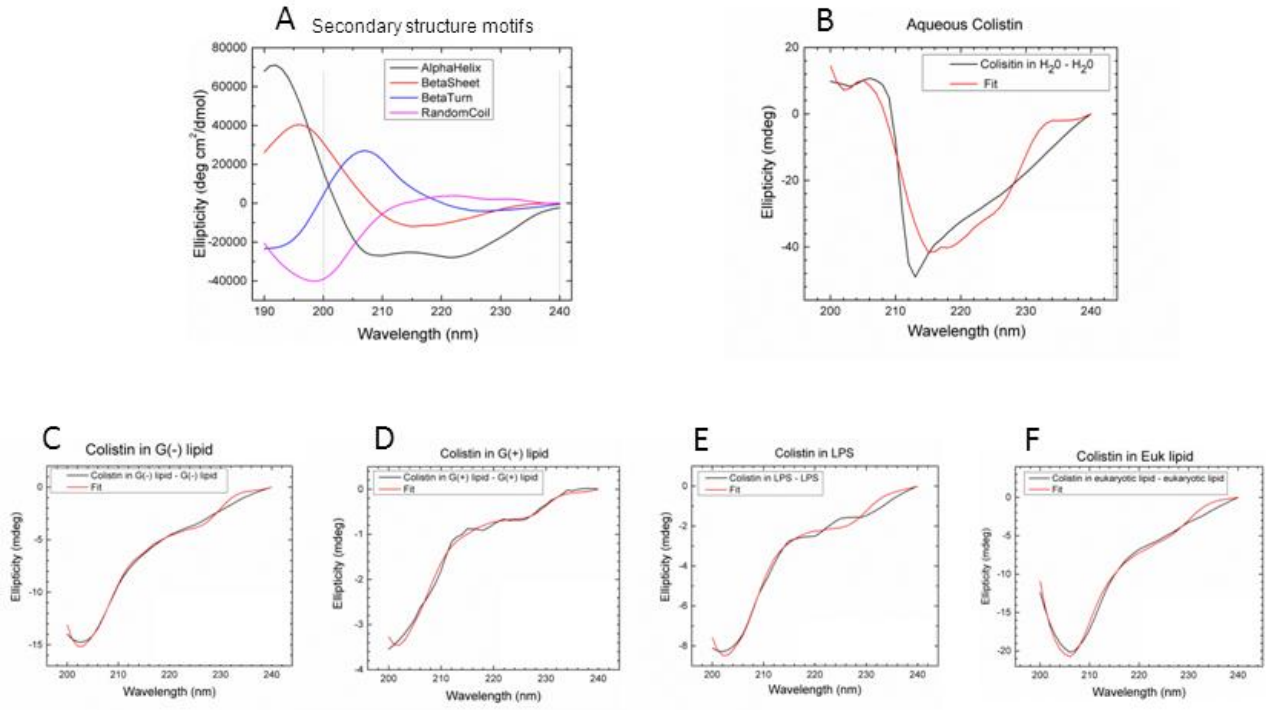

Figure S2. Circular dichroism results. A. Secondary structure motifs from Brahms & Brahms (1), used to fit the CD data between 200 and 240 nm with linear least-squares fitting. B. Colistin in the aqueous phase. C. Colistin in G(-) membrane mimic. D. Colistin in G(+) membrane mimic. E. Colistin in LPS membrane mimic. F. Colistin in Euk membrane mimic. For B-F, data are shown as black lines, fits as red lines. Appropriate background scans were subtracted for each sample. See Table 1 in main paper for motif percentages.

Ellipticity data were collected with a Jasco 715 at 37 ^{o}C in the Center for Molecular Analysis in the Chemistry Department at Carnegie Mellon University. For data analysis, a hyperplane routine supplied by OriginLab Corporation fitted the data over the wavelength range 200 to 240 nm. Hyperplane uses linear least squares to determine the unitless coefficients of the linear combination of the four structural motifs (Fig. S2A) provided by the data set in Ref. (1) using the equation y=A0+(A1*x1)+(A2*x2)+(A3*x3)+(A4*x4). The wavelength range 200 to 240 nm was chosen since it avoids the artefact that the alpha-helix can be fit quite well by the other three motifs if data from 190 to 240 nm are used. Brahms & Brahms (1) used the following reference spectra: beta-turn, poly-$(Ala_2\text{-}Gly_2)_n$. The beta-turn structure is representative of type I and type II, as confirmed by electron microscopy and x-ray diffraction. They refer to an earlier publication (2), that focused on poly-$(Ala_2\text{-}Gly_2)_n$. Alpha-helix was obtained from sperm whale myoglobin in 0.1M NaF pH 7, beta-pleated sheet, poly(lys+-Leu-Lys+-Leu) in 0.5 M NaF at pH 7, and random coil, poly(Pro-Lys+-Leu-Lys+-Leu) in water. The motifs were hand-digitized by Dr. Norma Greenfield from Ref. (1) and placed on this WEBsite: http://rwjms.rutgers.edu/research/cdf/experimental/other.html, where they were retrieved and used in this work. The concentrations of protein used in Ref. (1) are similar to those in this work. The Brahms & Brahms data set was found to be in good agreement with the Reed & Reed data set (3).

2. Details of LAXS data collection and analysis

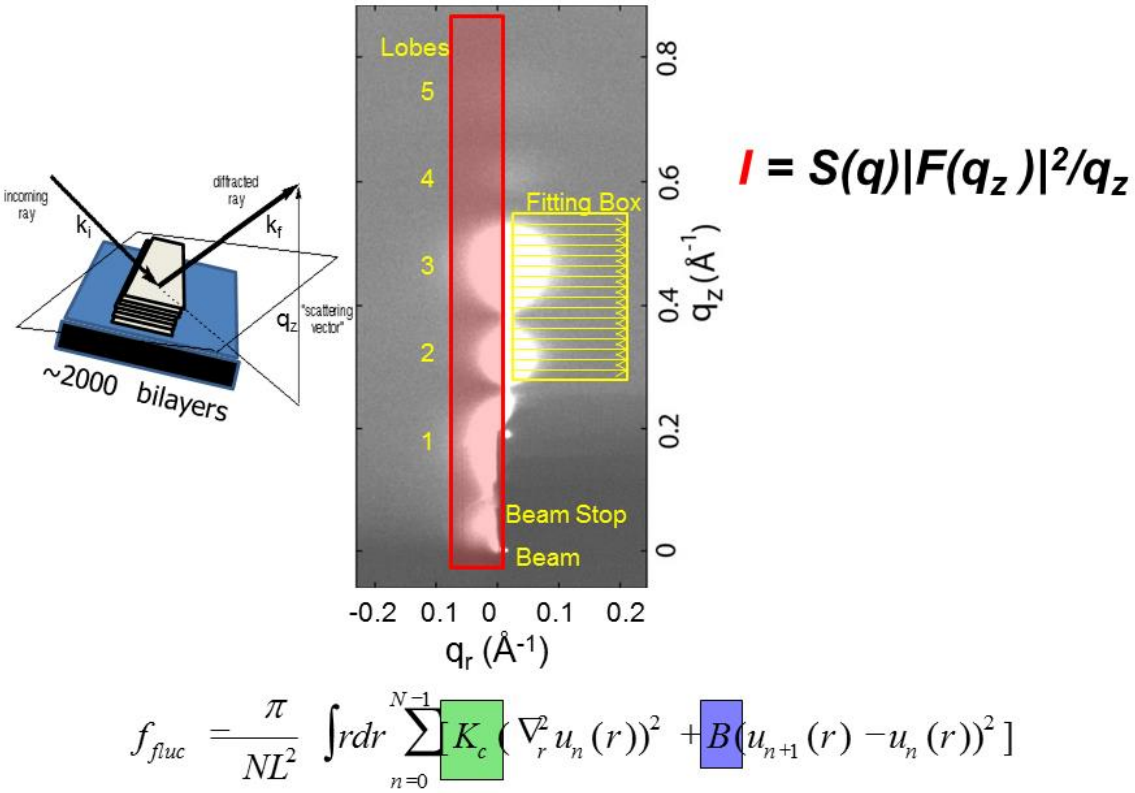

Figure S3. LAXS data collection and analysis. (Figure modified from Ref. (4)).

A stack of ~1800 bilayers on a silicon wafer is hydrated within a hydration chamber (5) (not shown), which causes membrane fluctuations near the fully hydrated condition (6, 7). The wafer is rotated from -1.6 to 7 degrees during the data collection to equally sample all scattered X-rays (30 sec dezingered scans at CHESS or 10 or 20 minute dezingered scans at CMU). Due to the fluctuations, large, nearly spherical "lobes" of diffuse X-ray scattering are produced (numbered in Fig. S3). These fluctuations are quantitated by measuring the fall-off in lobe intensity in the q_r direction in the yellow fitting box shown (4). The fitting procedure is a non-linear least squares fit that uses liquid crystal theory and requires our proprietary software, NFIT. For this work, we used NFIT12.0.5. Usually 30 iterations are required for convergence. By fitting to the free energy functional (equation at bottom of Fig. S3), the structure factor S(q), the bending modulus K_C and the compression modulus B are obtained. Subsequently, these parameters are fixed and the fit is carried out one additional time, fitting the area under the red slice. The result is the form factor, $F(q_z)$, obtained from the corrected scattering intensity (equation on the right in Fig. S3). q_z in this equation is the Lorentz polarization factor. The form factor obtained is then used to fit via the Fourier transform to a model of an electron density profile that uses Gaussians and error functions for the various membrane components. The computer program that carries out this fitting was written by Dr. Norbert Kučerka and is called the Scattering Density Profile (SDP) method (8). One important input to the SDP program is the lipid molecular volume, which is measured as described in Materials and Methods. Densities were measured for the individual membrane mimics and for colistin and appear in Table S1. When electrons are counted, then the Y-axis can be expressed as absolute electron density (e/Å^3).

The headgroup molecular volume is estimated by adding fractional volumes of a PC lipid (9), a PE lipid (10), a PG lipid(11), a TOCL lipid(12), Lipid A(13) and components (10) (see Table S1). The constraints used in the SDP fitting were the Gaussian width of the methyl trough (2-5 Å) and the distance between the carbonyl group position and the hydrocarbon edge (D_C) (1.3 Å). The SDP program yields many structural parameters, including bilayer thickness (D_{HH}, $2D_C$) and area/lipid A_L.

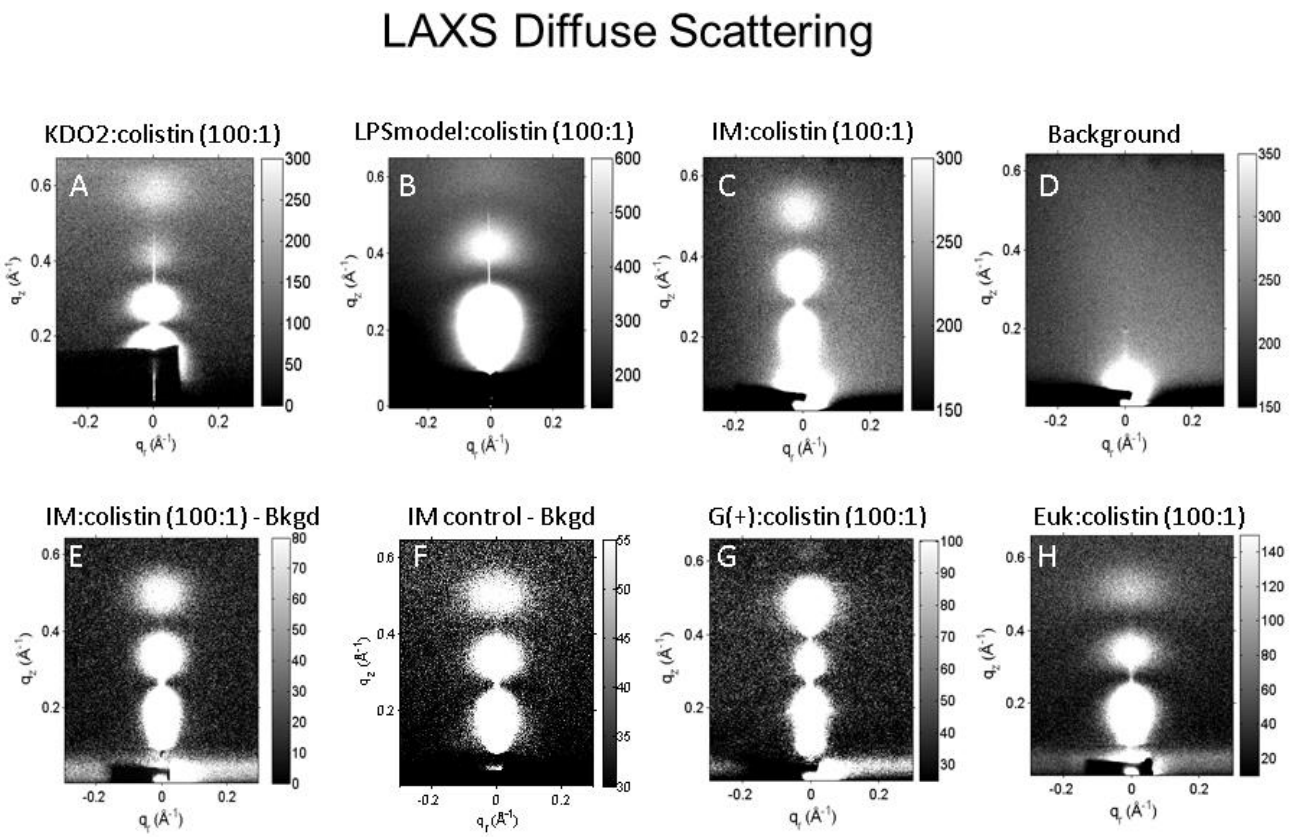

Figure S4. LAXS data collected at 55 °C at CHESS (A), 37 °C at CHESS (B) and 37 °C at CMU (C-H) of membrane mimics with 100:1 lipid:colistin molar ratio. A. KDO2, B. LPS model, C. G(-) IM, D. typical background scan, E. IM – background, F. IM control (no colistin) – background, G. G(+) membrane, H. Euk model. In A, the beam stop (dark rectangle) covers the beam and the first two lamellar orders, while in B-H, the beamstop covers only the beam near the bottom center of each image. The thin, white vertical line in A and B is the X-ray reflectivity from the underlying silicon wafer. Greyscale has been chosen to highlight the diffuse scatter in order to compare samples. All of these samples were fully hydrated as judged by the fact that the D-spacings were either very large (sample is unbinding) or had reached the largest value. The D-spacings for these samples are: A. 144 Å, B. 230 Å, C. 240 Å, E. 240 Å, F. 124 Å, G. 116 Å, H. 67 Å.

Fig. S4 shows typical raw LAXS data from oriented, fully-hydrated stacks of membrane mimics containing colistin. The concentration of lipid:peptide molar ratio (100:1) was chosen for this comparison. For data analysis, backgrounds were first subtracted and the images were symmetrized. An example of a background file is also shown in S4D. The background file was collected by setting the angle of X-ray incidence α = -2.4 degrees. At this angle, the data result from all extraneous scatter from the chamber including the beam overflowing the beamstop. Two examples of files with background subtracted are S4E and S4F. An image of a control sample (S4F), G(-) IM without added colistin, is shown for comparison. Visually, there is little difference between S4E and S4F, but their K_C values are different.

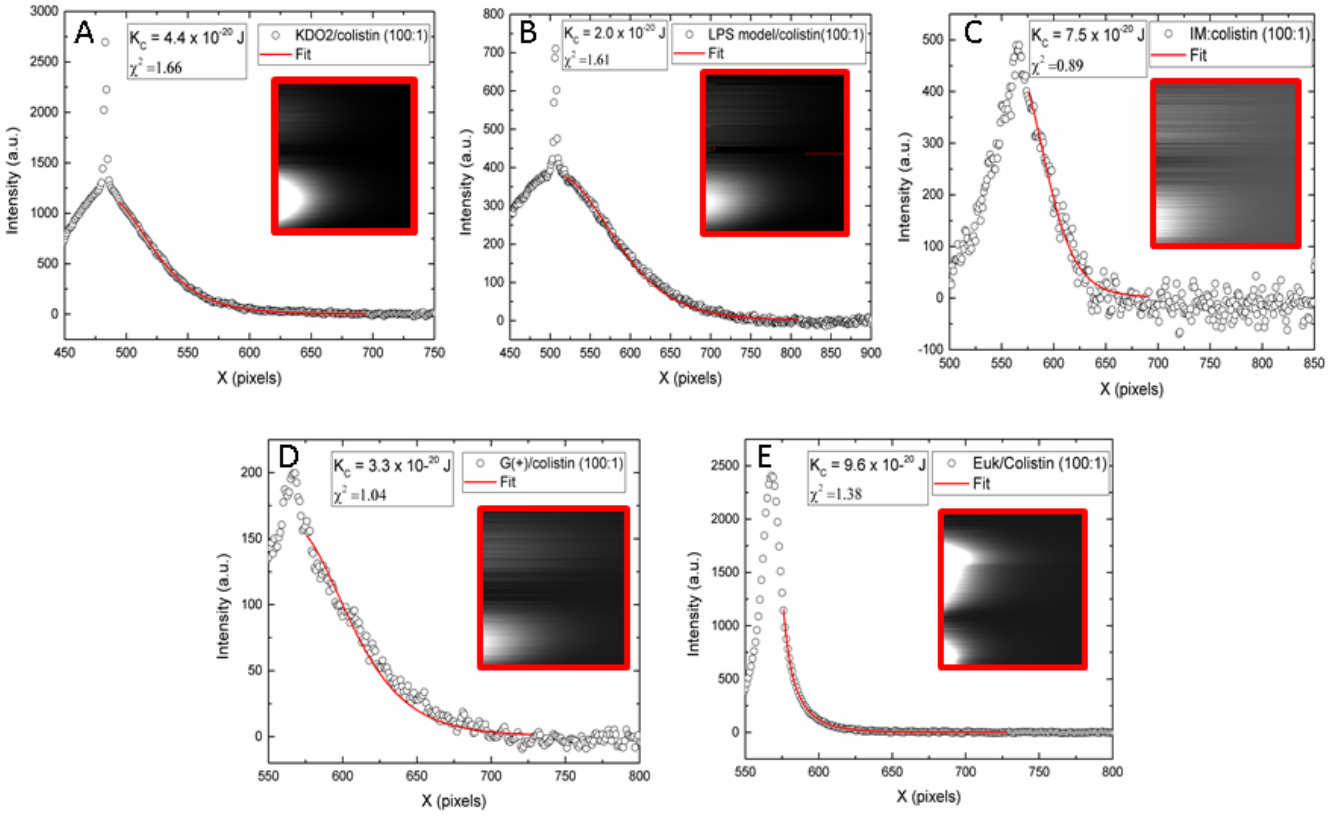

Figure S5. Fits to the liquid crystal diffuse scattering theory shown in Fig. 3 for the five samples in Fig. 4. A. KDO2/colistin (100:1), B. LPS model/colistin (100:1), C. IM:colistin (100:1), D. G(+)/colistin (100:1), E. Euk/colistin (100:1). The 2D images in the red boxes are the fits to the X-ray data in the fitting box shown in Fig. S3. The black open circles result from taking a q_r slice (width 20) at the same position as the highest intensity in the fitted boxes above (red outline). The fits to the data are shown as red lines, which overlay the intensity data fairly well. The chi-square, or goodness of fit, is shown in the legends on the graphs. These fits are typical of most of the data in this study.

Table S1. Volumes of membrane mimic controls and resulting area/lipid A_L.

Sample	**V_L (Å^3)**	**V_{HG} (Å^3)**	**A_L (Å^2)**
KDO2	3420[a]	1371[a]	169
LPS model	3705[a]	1686[a]	223
G(-) IM	1194	259	63.1
Eukaryotic	1108[b]	318	55.2[c]
G(+)	1213	274	66.3
Colistin (aqueous)	1573		

[a]These volumes were calculated based on LipidA volume from MD simulation (13) plus additional component groups with known volumes (10, 14).
[b]Includes cholesterol. [c]Lipid area (no cholesterol).

3. Details of WAXS data collection and analysis

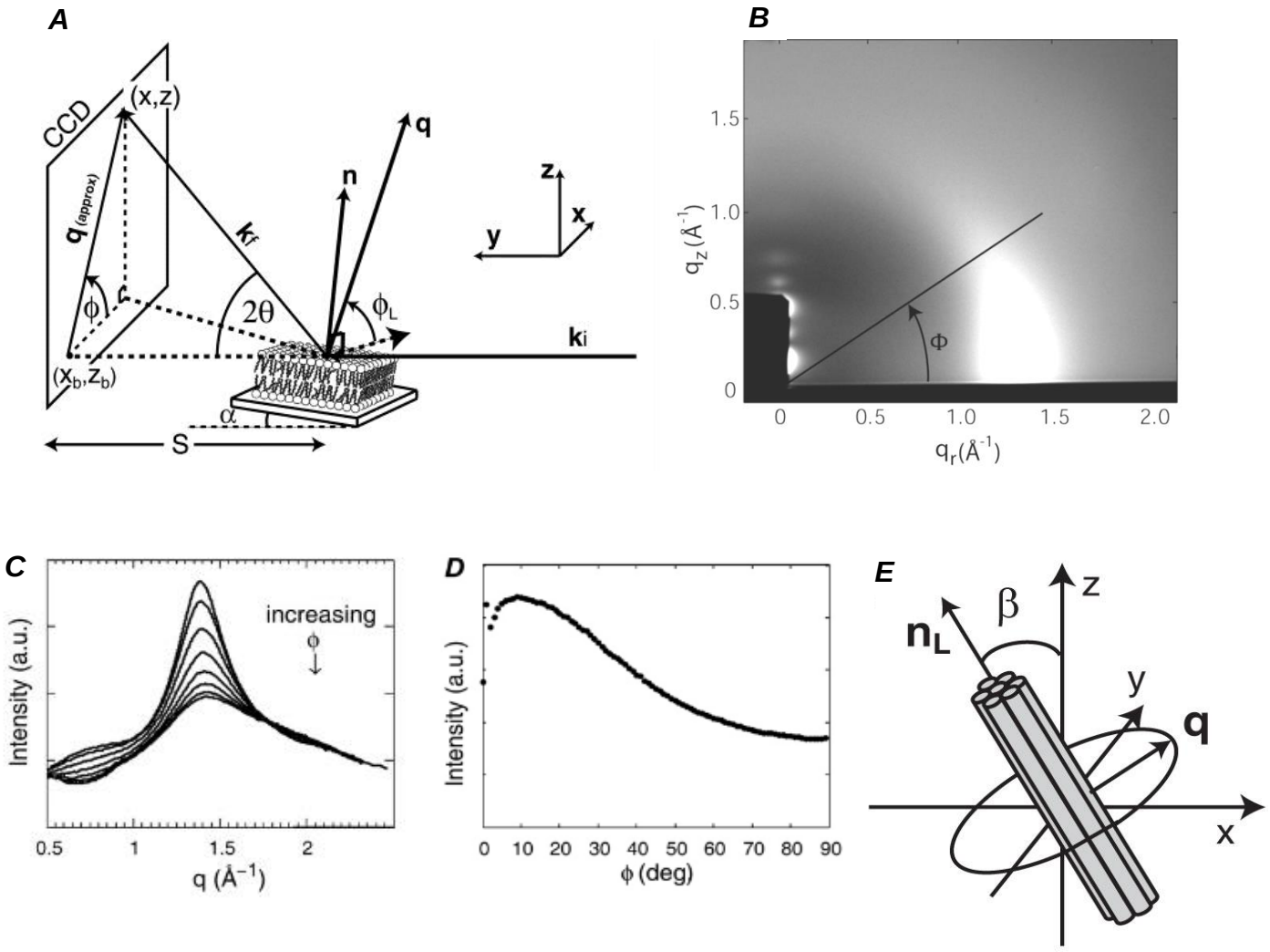

Figure S6. WAXS data collection and analysis. A. Scattering geometry, B. WAXS scattering from a well-ordered sample with background subtracted, C. WAXS intensity as a function of φ angle in 10 degree increments starting at the equator, D. Continuous WAXS intensity as a function of φ angle integrated from 1.2 to 2.2 Å^{-1} in q_r, E. Chain scattering model used to fit to WAXS intensity in D., F. Equation for determination of S_{xray}. Figure adapted from Mills et al. Ref. (15).

In order to obtain WAXS data, the same sample that was hydrated in LAXS is then X-rayed with the CCD detector close to the sample (see S-distances in main paper). Instead of rotating the wafer continuously as in LAXS, two pictures are taken: $\alpha = +0.5$ degrees and $\alpha = -0.5$ degrees. Both are dezingered, 30 second scans (CHESS), or dezingered 10 minute scans (CMU), which are then subtracted from each other. This procedure removes all extraneous scatter due to the mylar chamber windows and shadows. The scattering geometry is shown in Fig. S6A. The chain-chain correlation appears as strong diffuse scatter emanating upwards from the equator in a radial fashion around the φ angle; an example is shown in Fig. S6B. The fall-off in this diffuse intensity around the φ angle yields information about chain order; a steep fall-off, such as shown in Fig. S6B, indicates well-ordered chains, while a more continuous fall-off indicates less ordered chains. In order to carry out the analysis which quantitates the chain orientational order, a sector plot is first made by integrating in 10 degree pie sectors the WAXS intensity starting at the equator. An example of the resulting plot is shown in Fig. S6C. The q_r position of the maximum intensity is used to calculate the interchain d-spacing as $2\pi / q_r = d$. The sector plot is also used to determine the q_r range over which the WAXS intensity will be integrated, which is usually from ~1.2 to ~2.2 $Å^{-1}$. The WAXS intensity is then integrated as a function of φ over the chosen q_r range resulting in the intensity plot shown in Fig. S6D. In the chain scattering model shown in Fig. S6E, long thin rods are locally well aligned along the local director n_L, with orientation described by the angle β. For each grain (group of rods), scattering is permitted only at right angles to n_L. While acyl chains from lipids in the fluid phase are not long cylinders as shown, this model allows the cylinders to tilt (β) to approximate chain disorder. From the fit of the intensity data as a function of φ angle to the liquid crystal theory (15), we obtain S_{xray} using the equation in Fig. S6F, as well as the RMSE (root mean square error), which indicates the goodness of the fit. The order parameter for hydrocarbon chains obtained with WAXS (S_{xray}), although quantitatively lower than S_{CD} from NMR experiments, is able to detect different acyl chain order states in fluid lipid phases as previously shown (15, 16). The fitting is accomplished with a Matlab computer program written by Dr. Thalia Mills and Dr. Gil Toombes. Many more details about this WAXS analysis can be found in Ref. (15) and in the six Supplementary Material sections published in the Biophysical Journal in 2008. Fig. S7 shows WAXS data obtained from the same samples as for the LAXS data in Fig. S4. Fig. S8 shows fits of the theory to the WAXS data shown in Fig. S7.

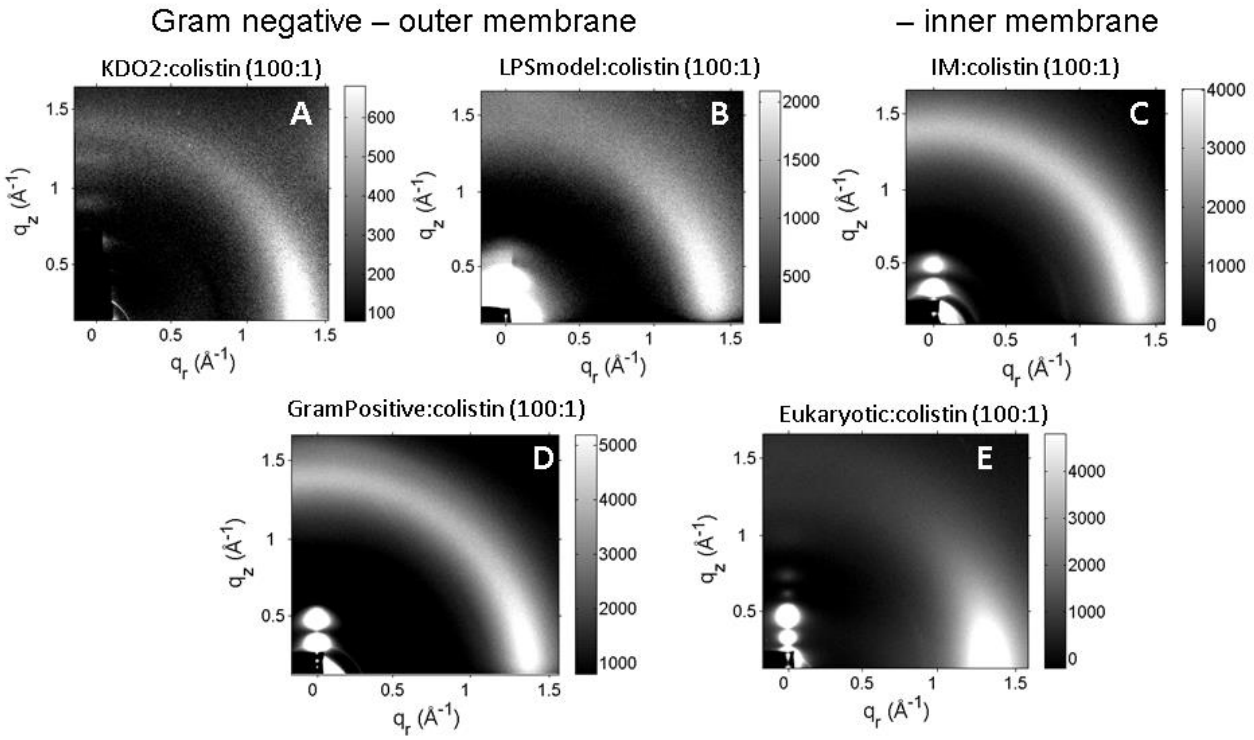

Figure S7. WAXS data collected at 37 ºC at CHESS (B-E) or 55 ºC (A) of membrane mimics at 100:1 lipid:colistin molar ratio. A. KDO2, B. LPS model, C. G(-) IM, D. G(+) membrane, E. Eukaryotic membrane. In A, the beam stop (dark rectangle) covers most of the shrunken LAXS pattern, while in B-E, the beamstop covers one (B) or two (C-E) lamellar orders in the small LAXS pattern near the lower left of the image.

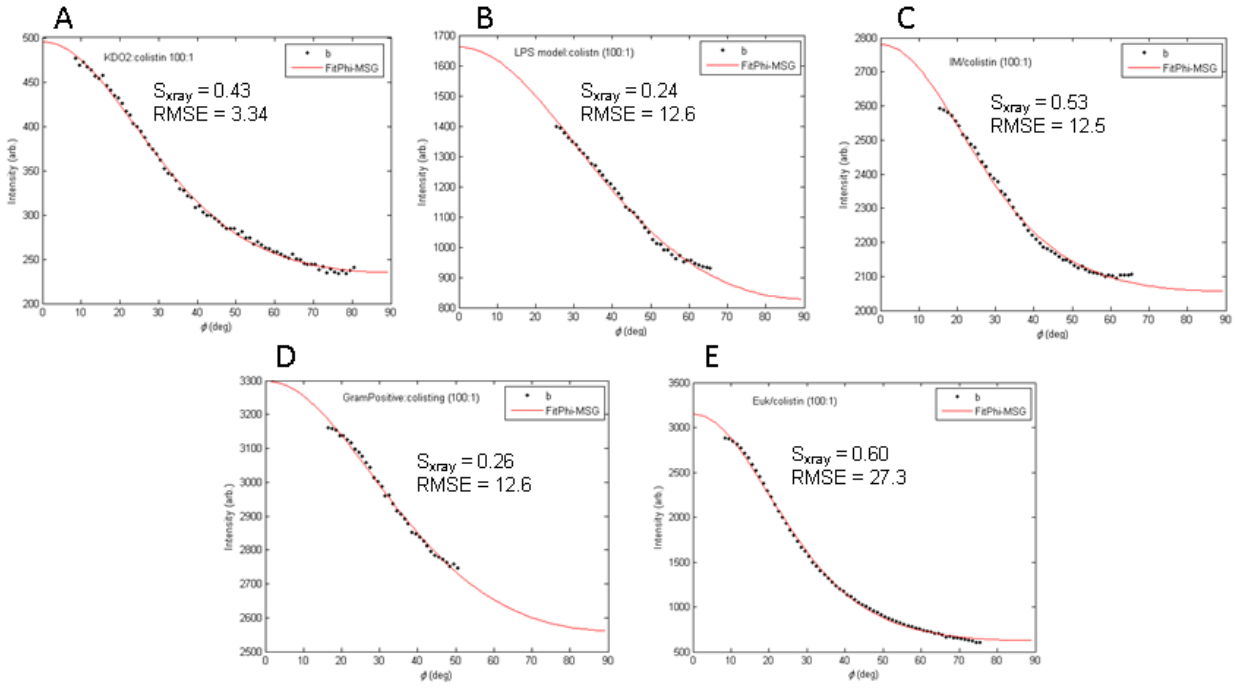

Figure S8. Fits of the WAXS liquid crystal theory shown in Fig. S6E,F to the WAXS data shown in Fig. S7 of membrane mimics at 100:1 lipid:colistin molar ratio. A. KDO2, B. LPS model, C. G(-) IM, D. G(+), E. Eukaryotic.

Details of neutron reflectivity

Details of the vesicle fusion method were described in the main paper. Basically, osmotic pressure causes the small unilamellar vesicles (SUVs) that are attached to the 3" silicon wafer to burst, thus forming the single bilayer shown in Fig. S9A. Rinsing completely removes the salt solution. The resulting bilayer is termed a sparsely tethered bilayer (17) since the tethers from the gold substrate are separated by 2-3 lipid molecules.

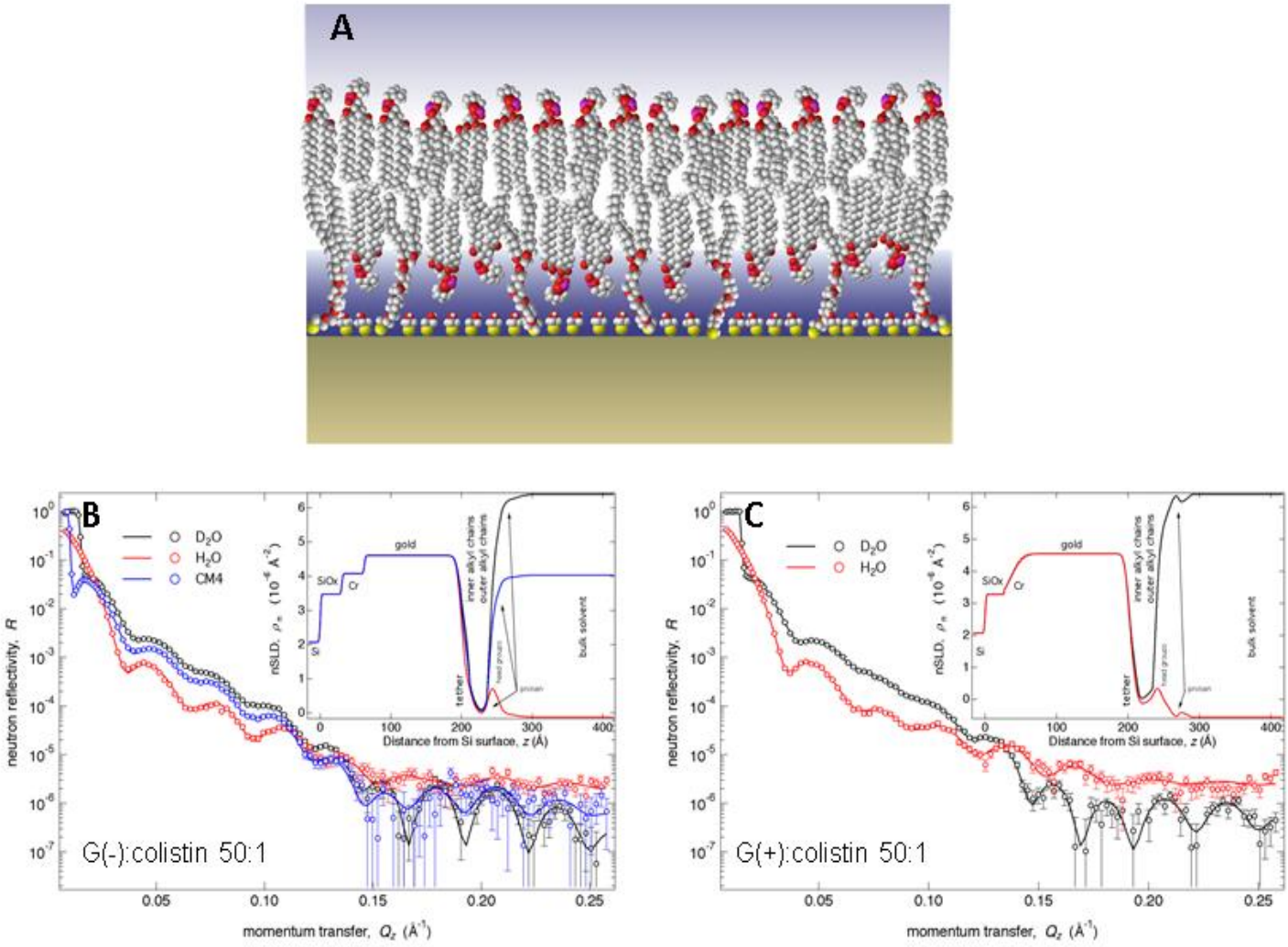

Figure S9. A. Sparsely tethered bilayer without peptide, cartoon adapted from Ref. (18). B. G(-) inner membrane mimic POPE:POPG:TOCL (7:2:1), neutron reflectivity curves (open circles) and best fits (solid lines). Legend indicates contrast solvents used, where CM4 is 67% D_2O and 33% H_2O with nSLD of $4e^{-6}$ $Å^{-2}$. (Inset: Best fit neutron scattering length density profile). C. G(+) membrane mimic POPG:POPE:DOTAP:TOCL (6:1.5:1.5:1), neutron reflectivity curves at two solvent contrasts and corresponding profile in inset. Both samples contained 50:1 lipid:colistin molar ratios.

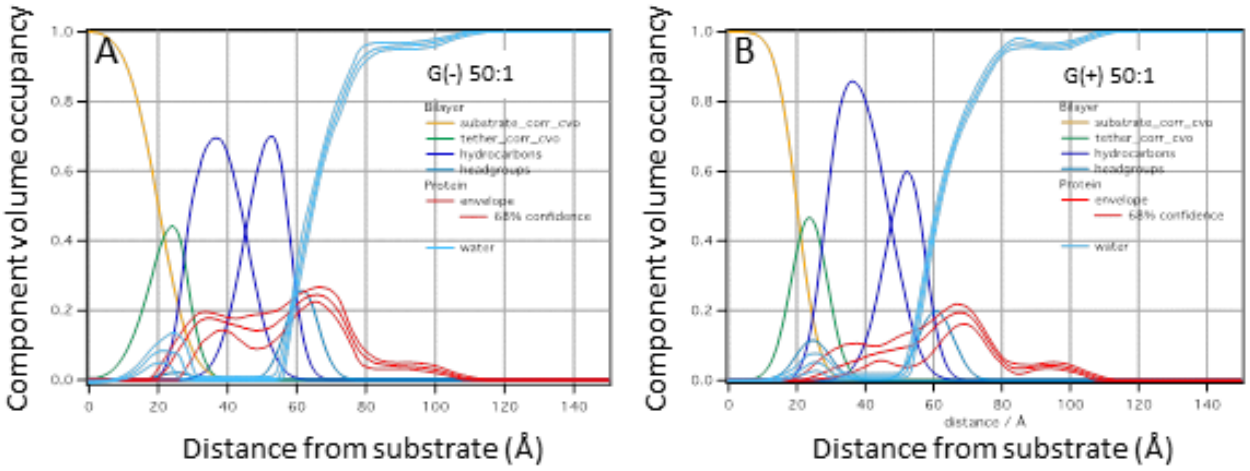

Figure S10. Component volume occupancy vs. distance from substrate of A. G(-) inner membrane and B. G(+) membrane mimics with 50:1 lipid:colistin molar ratio. The 1D-structural profile along the lipid bilayer normal was modeled using a composition space model (19). Median bilayer distributions and median protein profile with 68% confidence limits are shown. These data are also shown in a different format in Fig. 4 in the main paper.

Table S2. Fitting parameters for G(-) membrane mimic with colistin (50:1 molar ratio).

Parameter	Median ± 68% confidence
Tether thickness	9 ± 1 Å
Average hydrocarbon thickness per lipid leaflet	14 ± 3 Å
Area per lipid, outer leaflet	70 ± 20 Å^2
Bilayer completeness	99 ± 1 %
Amount of membrane-associated protein	10.1 ± 0.8 Å^3/Å^2
Fraction of protein in hydrocarbons	0.43± 0.04
Fraction of protein in outer headgroups	0.21 ± 0.03
Fraction of protein in bulk solvent	0.31 ± 0.03

Table S3. Fitting parameters for G(+) membrane mimic with colistin (50:1 molar ratio).

Parameter	Median ± 68% confidence
Tether thickness	8.5 ± 0.3 Å
Average hydrocarbon thickness per lipid leaflet	14 ± 3 Å
Average area per lipid	80 ± 20 Å^2
Bilayer completeness	99 ± 1 %
Amount of membrane-associated protein	6.7 ± 0.8 Å^3/Å^2
Fraction of protein in hydrocarbons	0.31± 0.06
Fraction of protein in outer headgroups	0.23 ± 0.05
Fraction of protein in bulk solvent	0.45 ± 0.05

Selected median model parameters and 68% confidence limits are shown in Tables S2 and S3.

4. Comparing experimental area/lipid A_L with MD simulation.

It is of interest to compare A_L determined using diffuse scattering methods to A_L determined by MD simulation, where many molecular details are observed. In Table S4, experimental A_L's are compared to A_L's obtained from MD simulations. As shown, there is a wide variability, which could be due to experimental conditions, and duration and parameters of the simulations. Another investigation simulated the binding of the related polymyxin B to both Lipid A and KDO2 bilayers, but A_L's were not published (20). A_L remains a central quantity for comparing simulation to experiment.

Table S4. Comparison of Experimental and Simulated A_L

Reference	A_L ($Å^2$)
X-ray (this work) (KDO2)	169
MD simulation (21) (lipid A)	168
X-ray (22) (LPS)	156
MD simulation (13) (lipid A)	151.5
MD simulation (23) (LPS)	130

SUPPORTING REFERENCES

1. Brahms, S., and J. Brahms. 1980. Determination of protein secondary structure in solution by vacuum ultraviolet circular-dichroism. J Mol Biol 138:149-178.
2. Brahms, S., J. Brahms, G. Spach, and A. Brack. 1977. Identification of beta, beta-turns and unordered conformations in polypeptide-chains by vacuum UV circular-dichroism. P Natl Acad Sci USA 74:3208-3212.
3. Reed, J., and T. A. Reed. 1997. A set of constructed type spectra for the practical estimation of peptide secondary structure from circular dichroism. Anal Biochem 254:36-40.
4. Tristram-Nagle, S., and J. F. Nagle. 2004. Lipid bilayers: thermodynamics, structure, fluctuations, and interactions. Chem Phys Lipids 127:3-14.
5. Kucerka, N., Y. F. Liu, N. J. Chu, H. I. Petrache, S. T. Tristram-Nagle, and J. F. Nagle. 2005. Structure of fully hydrated fluid phase DMPC and DLPC lipid bilayers using X-ray scattering from oriented multilamellar arrays and from unilamellar vesicles. Biophys J 88:2626-2637.
6. Liu, Y. F., and J. F. Nagle. 2004. Diffuse scattering provides material parameters and electron density profiles of biomembranes. Phys Rev E 69:040901(R).
7. Lyatskaya, Y., Y. Liu, S. Tristram-Nagle, J. Katsaras, and J. F. Nagle. 2001. Method for obtaining structure and interactions from oriented lipid bilayers. Physical review. E, Statistical, nonlinear, and soft matter physics 63:011907.
8. Kucerka, N., J. F. Nagle, J. N. Sachs, S. E. Feller, J. Pencer, A. Jackson, and J. Katsaras. 2008. Lipid bilayer structure determined by the simultaneous analysis of neutron and X-ray scattering data. Biophys J 95:2356-2367.
9. Tristram-Nagle, S., Y. F. Liu, J. Legleiter, and J. F. Nagle. 2002. Structure of gel phase DMPC determined by X-ray diffraction. Biophys J 83:3324-3335.
10. Nagle, J. F., and S. Tristram-Nagle. 2000. Structure of lipid bilayers. Bba-Rev Biomembranes 1469:159-195.
11. Pan, J. J., F. A. Heberle, S. Tristram-Nagle, M. Szymanski, M. Koepfinger, J. Katsaras, and N. Kucerka. 2012. Molecular structures of fluid phase phosphatidylglycerol bilayers as determined by small angle neutron and X-ray scattering. Bba-Biomembranes 1818:2135-2148.
12. Boscia, A. L., B. W. Treece, D. Mohammadyani, J. Klein-Seetharaman, A. R. Braun, T. A. Wassenaar, B. Klosgen, and S. Tristram-Nagle. 2014. X-ray structure, thermodynamics, elastic properties and MD simulations of cardiolipin/dimyristoylphosphatidylcholine mixed membranes. Chem Phys Lipids 178:1-10.
13. Murzyn, K., and M. Pasenkiewicz-Gierula. 2015. Structural properties of the water/membrane interface of a bilayer built of the E. coli lipid A. J Phys Chem B 119:5846-5856.
14. Molecular Modeling Pro
15. Mills, T. T., G. E. S. Toombes, S. Tristram-Nagle, D. M. Smilgies, G. W. Feigenson, and J. F. Nagle. 2008. Order parameters and areas in fluid-phase oriented lipid membranes using wide angle x-ray scattering. Biophys J 95:669-681.
16. Mills, T. T., S. Tristram-Nagle, F. A. Heberle, N. F. Morales, J. Zhao, J. Wu, G. E. S. Toombes, J. F. Nagle, and G. W. Feigenson. 2008. Liquid-liquid domains in bilayers detected by wide angle x-ray scattering. Biophys J 95:682-690.

17. Barros, M., F. Heinrich, S. A. Datta, A. Rein, I. Karageorgos, H. Nanda, and M. Lösche. 2016. Membrane Binding of HIV-1 Matrix Protein: Dependence on Bilayer Composition and Protein Lipidation. Journal of virology 90:4544-4555.
18. McGillivray, D. J., G. Valincius, D. J. Vanderah, W. Febo-Ayala, J. T. Woodward, F. Heinrich, J. J. Kasianowicz, and M. Lösche. 2007. Molecular-scale structural and functional characterization of sparsely tethered bilayer lipid membranes. Biointerphases 2:21-33.
19. Heinrich, F., and M. Lösche. 2014. Zooming in on disordered systems: Neutron reflection studies of proteins associated with fluid membranes. Bba-Biomembranes 1838:2341-2349.
20. Berglund, N. A., T. J. Piggot, D. Jefferies, R. B. Sessions, P. J. Bond, and S. Khalid. 2015. Interaction of the antimicrobial peptide polymyxin B1 with both membranes of E. coli: a molecular dynamics study. PLoS computational biology 11:e1004180.
21. Wu, E. L., O. Engstrom, S. Jo, D. Stuhlsatz, M. S. Yeom, J. B. Klauda, G. Widmalm, and W. Im. 2013. Molecular dynamics and NMR spectroscopy studies of E. coli lipopolysaccharide structure and dynamics. Biophys J 105:1444-1455.
22. Snyder, S., D. Kim, and T. J. McIntosh. 1999. Lipopolysaccharide bilayer structure: effect of chemotype, core mutations, divalent cations, and temperature. Biochemistry-Us 38:10758-10767.
23. Soares, T. A., Straatsma, T.P. 2008. Assessment of the convergence of molecular dynamics simulations of lipopolysaccharide membranes. Molecular Simulations 34:295-307.